# NOTICE TO BORROWERS



The author of this dissertation is

William M. Lee
6105 Blodgett Ave.
Downers Grove, Illinois 60516

The director of this dissertation is

Dr. Gus A. Petitt
Department of Physics and Astronomy
College of Arts and Sciences

# A Measurement of the Nuclear Dependence of $J/\psi$ and $\psi'$ Production

A Dissertation

Presented in Partial Fulfillment of Requirements for the
Degree of Doctor of Philosophy
in the College of Arts and Sciences
Georgia State University

1999

by
William M. Lee

Committee:

Dr. Gus A. Petitt, Chair

Dr. Xiaochun He, Member

Dr. Steven T. Manson, Member

Dr. Carl R. Nave, Member

Dr. William H. Nelson, Member

Dr. Paul J. Wiita, Member

Date

Dr. William H. Nelson, Chair
Department of Physics and Astronomy

# Abstract

A measurement of $J/\psi$ and $\psi'$ production has been performed for 800 GeV/c protons incident on nuclear targets of beryllium, iron, and tungsten over a very broad range in the kinematic variables, Feynman $x$ ($x_F$) and transverse momentum ($p_T$). Over $3 \times 10^6$ $J/\psi$'s and $10^5$ $\psi'$'s with $x_F$ between $-0.10$ and 0.93 and $p_T$ up to 4 GeV/c were observed. A reduction in the cross section per nucleon for the heavier nucleus as compared to the lighter nucleus, i.e. suppression, is observed for all $x_F$. This suppression is smallest for $x_F$ values less than 0.25 and increases for larger $x_F$. It is also strongest at small $p_T$. For the first time in p-A collisions, the $\psi'$ has been observed to be more greatly suppressed than the $J/\psi$ which occurs for $x_F$ near zero. At $x_F$ around 0.5, the suppression for the $\psi'$ becomes less than that for the $J/\psi$ while similar suppression is shown for larger values of $x_F$.

# Acknowledgements

It has been a pleasure to be a member of the FNAL E866/NuSea collaboration. Without the support and contributions of the many members of this group, I doubt that this dissertation would be finished today.

The FNAL E866/NuSea Collaboration

M.E. Beddo, C.N. Brown, T.A. Carey, T.H. Chang, W.E. Cooper,

C.A. Gagliardi, G.T. Garvey, D.F. Geesaman, E.A. Hawker, X.C. He,

L.D. Isenhower, D.M. Kaplan, S.B. Kaufman, D.D. Koetke, W.M. Lee,

M.J. Leitch, P.L. McGaughey, J.M. Moss, B.A. Mueller,

V. Papavassiliou, J.C. Peng, G. Petitt, P.E. Reimer, M.E. Sadler,

W.E. Sondheim, P.W. Stankus, R.S. Towell, R.E. Tribble, M.A. Vasiliev,

J.C. Webb, J.L. Willis, and G.R. Young

As usual there are those that have gone above and beyond the call of duty. I wish to thank Don Geesaman for providing me space at Argonne to finish my work. Paul Reimer has always been a good sounding board for my questions. Carl Gagliardi has

provided me with many useful improvements to this dissertation. I also wish to thank Chuck Brown for introducing me to FermiLab and the Meson East Hall. Thank you to my fellow graduate students, Eric, Rusty, and Ting for showing me the way, and to Jason, may you be close behind.

It was a great pleasure to work with Tom Carey and Paul Stankus on the level three trigger. You have been great friends. Thanks for helping me out whenever we would get together. I just wish that we would have gotten the trigger in sooner.

Mike Leitch has been my partner in the analysis of this data. I would like to thank him for his help in shuttling me out to Los Alamos. Thank you for your insight and teaching and for your time. Without your guidance I would probably still be working on the analysis.

I wish to thank my advisor Gus Petitt who stuck with me even after retirement. Good luck to you now that you can fully retire. I also wish to thank Xiaochun He for helping support and advise me after Gus retired.

Finally I wish to thank my wife, Malinda Hamann, and my children, Quentin and Benjamin, for not complaining too much as I traveled to FermiLab and Los Alamos. Quentin and Benjamin, thank you for making my life a joy. Malinda, thank you for all of your support and love.

# Contents

# List of Tables

# List of Figures

"There appears to be no mechanism for $J/\psi$ suppression in nuclear collisions except for the formation of a deconfining plasma"

- T. Matsui and H. Satz (1986)

# Chapter 1

# Introduction

Since the early 1980's, the East wing of the Meson area of Fermi National Accelerator Laboratory has housed the Meson-East spectrometer. This spectrometer was first used by Experiment 605 to detect single charged particles produced with high transverse momenta and high mass pairs of oppositely charged particles [1]. In 1985, the final run of E605, the spectrometer was mainly used as a high mass dimuon detector [2]. At the end of the decade, this spectrometer again came to life, this time for Experiment 772. E772 used the spectrometer in the dimuon configuration, this time to study the nuclear dependence of high mass dimuon pairs [3]. Shortly after E772 was run, the spectrometer was again recommissioned. In 1991, with the addition of silicon strip detectors and other improvements, Experiment 789 was used to observe $J/\psi$ production from beauty decays [4].

Finally in September of 1996, using the E772 configuration with an enhanced data acquisition system and a new trigger, the Meson-East spectrometer was again used for Experiment 866. The primary goal of the E866 experiment was to measure the $\bar{d}/\bar{u}$ asymmetry in the nucleon sea [5, 6, 7, 8]. Upon completion of this measurement several supplemental measurements were also made [9, 10], including a nuclear dependence measurement of $J/\psi$ and $\psi'$ production, performed in April 1997.

Ever since Matsui and Satz [11] predicted that $J/\psi$ suppression might be a possible signal of the Quark-Gluon Plasma, there have been many studies of the production of the $J/\psi$ on a variety of targets. These experiments (some of which will be discussed in the next chapter) have seen a suppression of $J/\psi$ production, but at energies below where a Quark-Gluon Plasma is expected to be formed. Some other explanation needs to be found. Energy loss effects [12, 13, 14, 15], intrinsic charm [16], shadowing [17], co-mover interaction [18], color-octet production [19], and other mechanisms have been proposed to explain the data. It is important to try to determine which of these effects, if any or all, are causing this suppression. If $J/\psi$ suppression is to be used as a tool to find the Quark-Gluon Plasma, then it needs to be understood in cold nuclear matter first.

Measurements of the nuclear dependence of $J/\psi$ and $\psi'$ production by E772 [20] had been limited by poor spectrometer acceptance in this mass range. So at a time when CERN NA50 was detecting an increased suppression in $J/\psi$ production in lead

on lead collisions [21], and the Relativistic Heavy Ion Collider was actively being built, E866 decided to improve upon the E772 measurement. With its greater acceptance and higher statistics, E866 provides a new insight into charmonia suppression.

# Chapter 2

# Background

In order to study the nuclear dependence of $J/\psi$ production, some of the history prior to E866 needs to be explored. The first portion of this chapter will review the important terms. Following this is a short list of experiments that provided much of the data before E866. Finally, some effects that have been theorized to interpret the data from these experiments will be explored.

## 2.1 Review

### 2.1.1 Charmonium

The $\psi$ particle [22] was first discovered in 1974 in $e^+e^-$ collisions at SLAC. Simultaneously, in collisions of 28 GeV protons on beryllium at Brookhaven, the $J$ particle [23]

was discovered. The $J$ and the $\psi$ were resolved to be the same particle, now known as the $J/\psi$. This meson with a mass of just under 3.1 GeV is the lowest-lying vector meson state (1S) of a bound $c$ quark and a $\bar{c}$ quark. A second resonance [24], the 2S, at a mass of 3.7 GeV was discovered at SLAC and named $\psi'$. This group of $c\bar{c}$ vector mesons is often called charmonium, and also includes the $\chi_c$ states which are the P orbital angular momentum states.

### 2.1.2 Nuclear dependence

If there were no nuclear dependence in the production of charmonia, then the cross-section for a target of atomic mass, A, should be related by the equation:

$$\sigma_{pA} = A\,\sigma_{pN} \tag{2.1}$$

where $\sigma_{pA}$ is the cross-section for the nuclear target and $\sigma_{pN}$ is the cross-section for a single nucleon. For $J/\psi$ production there is a nuclear dependence, often referred to as a nuclear suppression or just suppression. Nuclear suppression is a reduction in the cross-section per nucleon for targets with a larger atomic mass.

The best way to demonstrate the nuclear dependence is to observe the ratio of the cross-sections per nucleon for two targets. If there is no nuclear dependence, then the ratio should be equal to one.

Since different experiments use different targets, it is difficult to compare experiments when looking at ratios. Most experiments express the nuclear dependence with the parameter, $\alpha$, where $\alpha$ is defined by:

$$\sigma_{pA} = A^{\alpha}\,\sigma_{pN}. \tag{2.2}$$

If $\alpha$ is equal to one, then this equation is equivalent to Equation 2.1, and there is no nuclear dependence. Nuclear suppression would give a value of $\alpha$ less than one, while an $\alpha$ greater than one indicates an enhancement. In addition to providing a method for comparison between experiments, $\alpha$ also provides a single parameter for comparison when using multiple nuclear targets. There is no known theoretical reason for using the parameter $\alpha$, but as will be shown in Sections 2.2.2 and 2.2.3, $\alpha$ provides a reasonable parameterization of the data.

### 2.1.3 Kinematics

Since E866 is a high statistics experiment, our data may be divided into different kinematic regions in order to obtain a better understanding of the nuclear dependence. The kinematic variables that can be studied in E866 are mass, m; Feynman $x$, $x_F$; transverse momentum, $p_T$; and the Collins-Soper decay angles, $\theta$ and $\phi$. Of these, as will be seen throughout the rest of this chapter, $x_F$ and $p_T$ are the variables most

likely to exhibit nuclear effects, and hence are the most interesting to explore.

Feynman $x$ is defined as:

$$x_F = \frac{p_{||}}{p_{||}^{max}} \tag{2.3}$$

where $p_{||}$ is the longitudinal momentum of the $J/\psi$ in the center of mass frame, and $p_{||}^{max}$ is the maximum longitudinal momentum. So, $x_F$ can be thought of as the forward momentum fraction. Since $x_F$ is Lorentz invariant, it is useful for momentum comparisons. The transverse momentum is more obvious. It is simply the magnitude of the momentum component perpendicular to the beam direction.

## 2.2 Previous Experiments

$J/\psi$ production has been well studied with a variety of beams and energies. Knowledge gathered by the previous experiments already gives us a large amount of information about the nuclear dependence. It also provides motivation towards where more data should be obtained. While only a few of the previous experiments will be covered here, the majority of the known hadron-nucleus nuclear dependence is covered by these experiments.

### 2.2.1 CERN NA3

NA3 was designed to study dimuons at the CERN Super Proton Synchrotron (SPS). While the experiment was optimized to study high mass ($M_{\mu\mu} > 4$ GeV/$c^2$) dimuons, they still had a fairly good acceptance for $J/\psi$'s. NA3 used secondary beams of protons, antiprotons, pions, and kaons at momenta of 150, 200, and 280 GeV/c. The nuclear dependence was determined using liquid hydrogen and solid platinum targets.

NA3 was one of the first experiments to observe the $x_F$ dependence [25] as shown in Figure 2.1, which is a plot of the ratio of the cross-sections per nucleon for the platinum over hydrogen targets as a function of $x_F$. This figure also compares the pion induced production of $J/\psi$'s to that measured by protons at 200 GeV/c. The main feature of the $x_F$ dependence is the increased suppression of the $J/\psi$ for larger $x_F$. Figure 2.2 gives the same ratio as the previous figure, now plotted versus $p_T$. Here the ratio increases versus $p_T$. For $p_T$ greater than two GeV/c, an enhancement is seen as the ratio becomes greater than one.

### 2.2.2 FermiLab E772 and E789

FermiLab Experiment 772 measured the yield of $J/\psi$ and $\psi'$ for 800 GeV protons incident on deuterium, carbon, calcium, iron, and tungsten targets [20]. From Figure 2.3, E772's results demonstrate a suppression of the yield of $J/\psi$ and $\psi'$ versus mass number. The dashed curve in Figure 2.3 corresponds to the best fit with an $\alpha$

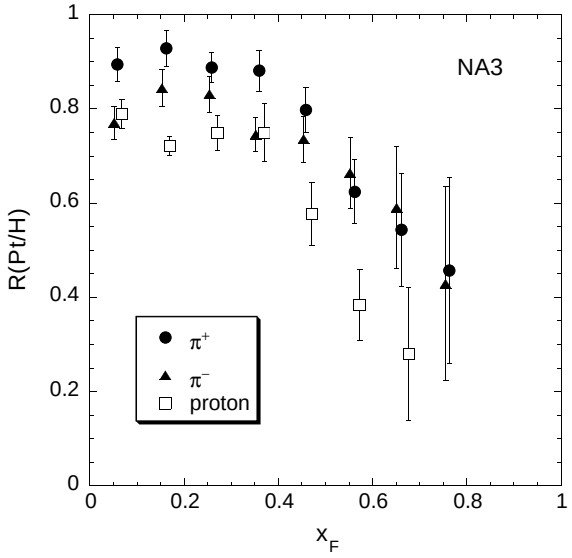


Figure 2.1: Ratios of the $J/\psi$ cross-section per nucleon for platinum over hydrogen versus $x_F$ for 200 GeV/c $\pi^+$, $\pi^-$, and proton NA3 [25] data.

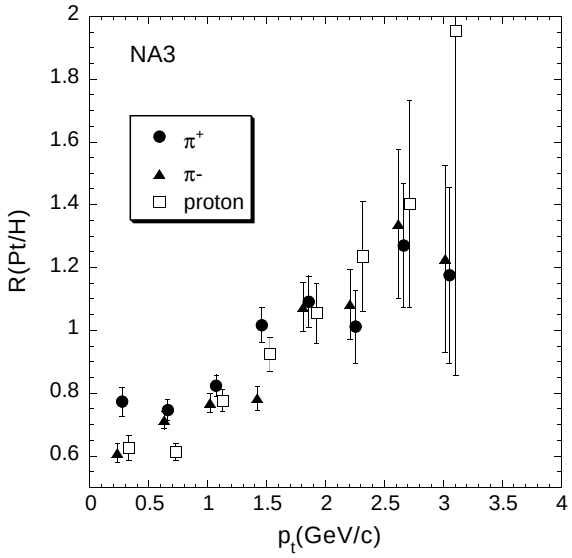


Figure 2.2: Ratios of the $J/\psi$ cross-section per nucleon for platinum over hydrogen versus $p_T$ for 200 GeV/c $\pi^+$, $\pi^-$, and proton NA3 [25] data.

of 0.92. This also shows that Equation 2.2 is an adequate, but not perfect, parameterization. The inset in the figure shows E772's dimuon invariant mass spectrum, which demonstrates that the $J/\psi$, the large peak on the far left of the spectrum, is on the edge of the mass acceptance. The peak just to the right of the $J/\psi$ is the $\psi'$, while the peak on the far right is the $\Upsilon$, a $b\bar{b}$ quark resonance. The dimuons between the $\psi'$ and the $\Upsilon$ are generated by the Drell-Yan process which is quark-antiquark annihilation creating a virtual photon which decays to a dilepton. E772 was the first experiment with adequate statistics and mass resolution to demonstrate the similar suppression between the $J/\psi$ and $\psi'$. Also shown in Figure 2.3 are the Drell-Yan (DY) cross-section ratios [3]. From these ratios, it can be seen that suppression in DY is minimal compared to that for the $J/\psi$.

The main purpose of E789 was to investigate the production of $b$-quarks via inclusive $b \rightarrow J/\psi \rightarrow \mu^+\mu^-$ decays [4]. In addition, E789 also used beryllium, carbon, and tungsten targets to study the nuclear dependence of $J/\psi$ production near $x_F = 0$ [26] and a thick beryllium insert along with the copper beam dump to measure the nuclear dependence for $x_F > 0.3$ [27]. The results can be seen in Figure 2.4 along with $x_F$ dependence from NA3 and E772. At large $x_F$, E772 also shows increasing suppression while E789 levels off. At smaller $x_F$ NA3 shows less suppression than E772 and E789.

Figure 2.5 shows the $p_T$ dependence for NA3, E772, and the small $x_F$ E789

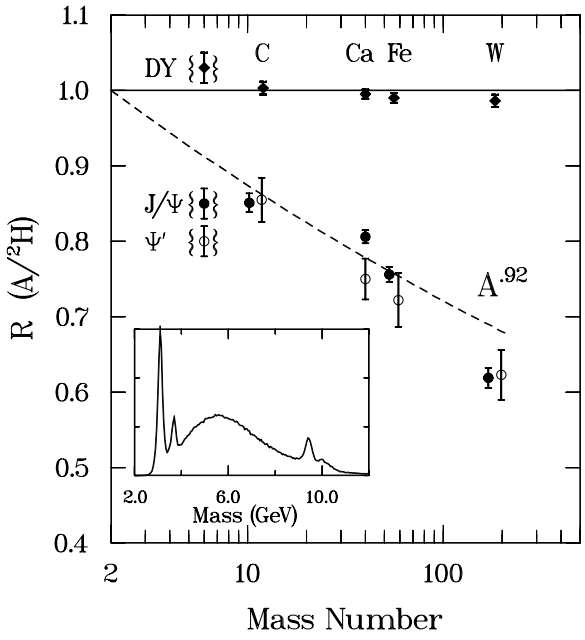


Figure 2.3: The ratio of heavy nucleus to deuterium integrated yields for the $J/\psi$ and $\psi'$ resonances. The ratios for the Drell-Yan continuum are also shown. The insert shows the dimuon invariant mass spectrum [20].

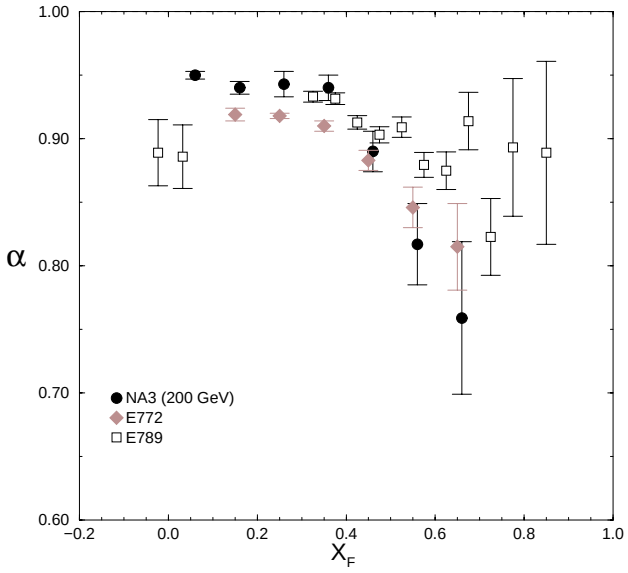


Figure 2.4: $\alpha$ versus $x_F$ for Experiments NA3 [25], E772 [20], and E789 [26, 27].

measurement. It is important to note the difference in $p_T$ coverage for the three experiments. This will be discussed in more detail later in Section 5.2.

E789 also made a measurement of the nuclear dependence of neutral $D$ mesons at an $x_F$ near zero [28]. At a mean $x_F$ of 0.031, $\alpha$ was $1.02 \pm 0.03$ (statistical) $\pm 0.02$ (systematic), which is consistent with no nuclear dependence. For experiments that explicitly reconstructed the $D$, E789 is the only measurement with proton induced $D$ meson production. Other experiments have measured the nuclear dependence induced by pions [29, 30]. These are also consistent with no nuclear dependence.

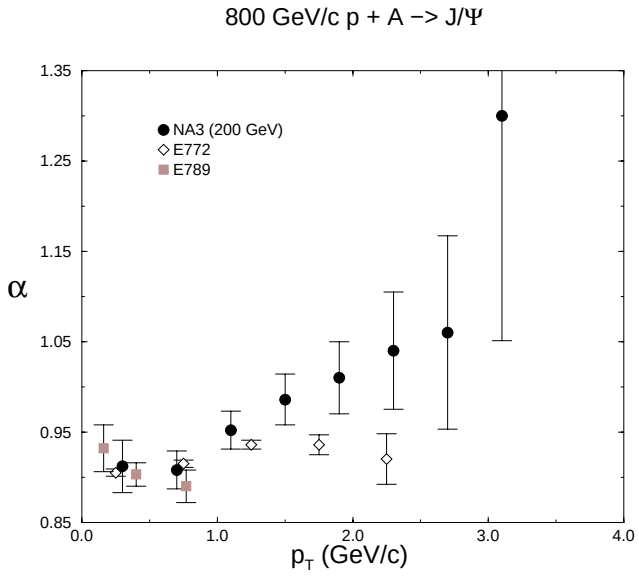


Figure 2.5: $\alpha$ versus $p_T$ for Experiments NA3 [25], E772 [20], and E789 [26].

### 2.2.3 NA38

The NA38 experiment was designed to study dimuon production in high energy nucleus-nucleus reactions. In order to establish a baseline for heavy ion studies, NA38 also studied proton nuclear interactions using carbon, aluminum, copper, and tungsten targets [31]. The kinematics of this data covered the small positive $x_F$ region and had good $p_T$ coverage from 0 to greater than 4 GeV/c. The absolute cross-sections per nucleon are shown in Figure 2.6 versus atomic mass. The data from the NA51 $pp$ and $pD$ reactions [32] are also shown. The dashed line in Figure 2.6 is a fit to the parameterization $A^\alpha$ for both sets of data, with $\alpha = 0.919 \pm 0.015$, which is same as E772. NA38 has also shown that the $J/\psi$ and $\psi'$ are equally suppressed

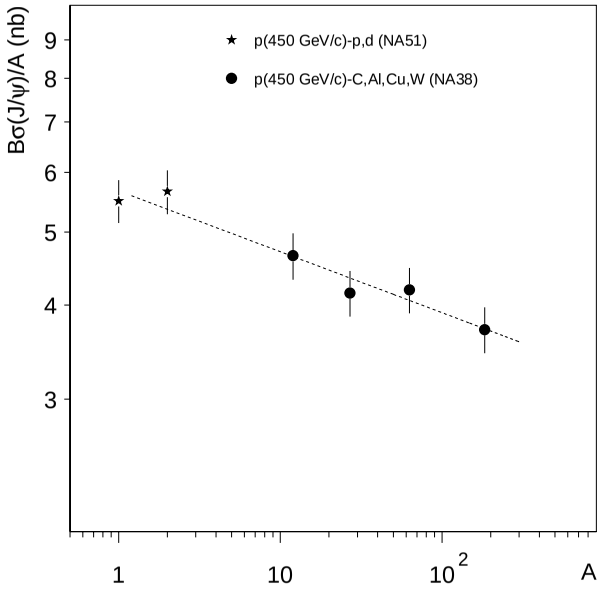


Figure 2.6: Absolute $J/\psi$ cross-sections per nucleon versus atomic mass for the NA38 and NA51 experiments. The line is a fit to $A^{\alpha}$. [31]

in proton-nucleus collisions, as shown in Figure 2.7. With the addition of data from other experiments of different energies and kinematics in the figure, as referenced in [31], it would appear that the $\psi'/J/\psi$ ratio is independent of $\sqrt{s}$ and the experiments kinematics.

## 2.3 Charmonia Production

In order to understand the nuclear effects that will be discussed in Section 2.4, it is important to have some understanding as to how the $J/\psi$ and $\psi'$ are produced. Generally, it is believed that a charmonia is produced in two steps. First the $c\bar{c}$ pair

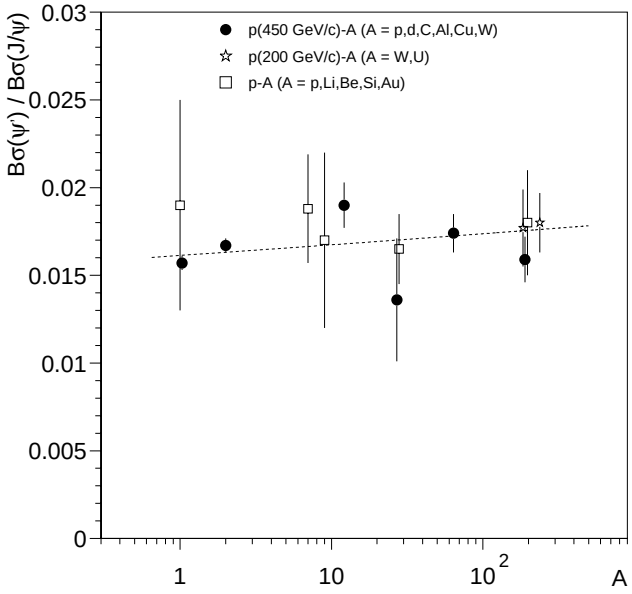


Figure 2.7: Ratio of cross-sections for the $\psi'$ over $J/\psi$ versus mass number. The closed circles come from the 450 GeV/c NA38 and NA51 data while the open points come from other experiments and energies as referenced in [31].

must be created. Then the $c\bar{c}$ pair must bind together, or hadronize, into some form of charmonium.

For E866 the $c\bar{c}$ is produced from colliding partons in the hadron collisions. The simplest forms for this are from gluon-gluon fusion, as shown in Figure 2.8, or from quark-antiquark annihilation, Figure 2.9. At high energies, gluon-gluon fusion is expected to be the main production mechanism for charmonia production, but at $x_F$ greater than 0.6, quark-antiquark annihilation may begin to dominate. This is shown in Figure 2.10, a prediction by Ramona Vogt [33] using the Color Evaporation Model [34] for the E866 kinematics. The $x_F$ crossover point changes slightly depending on the model, but can go as high as 0.8.

For many years, the color singlet model [35] was used to predict the probability of forming a $J/\psi$. In this model, a $c\bar{c}$ is produced as a point-like particle and a hard gluon must be radiated to achieve the color singlet state on a perturbative timescale. In 1996 the Collider Detector at FermiLab (CDF) experiment finished the first run of $p\bar{p}$ collisions. Later that year, the CDF collaboration published cross-sections [36] for high $p_T$ prompt $J/\psi$, an area where the predictions should be reliable. The result was that the color singlet model under predicted these cross-sections by a factor of 30.

This has led to a number of new models. Both a non-relativistic QCD approach [19] and a Color Evaporation Model [34] have been able to predict the CDF

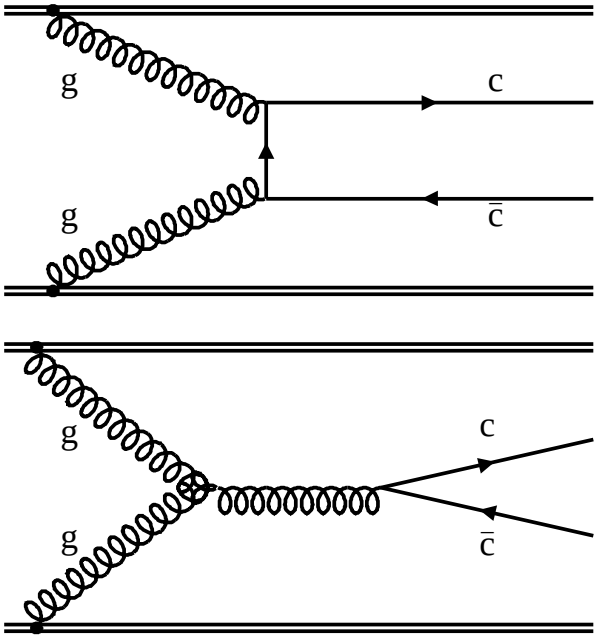


Figure 2.8: Charmonia production diagrams from gluon-gluon fusion.

data. Both of these models include the $J/\psi$ produced in a color octet state. In the color octet state the $c\bar{c}$ no longer needs to emit a hard gluon upon formation, and can emit soft gluons at a later time to hadronize.

E866 does not have the ability to distinguish prompt $J/\psi$'s from those produced from feed-down from the $\psi'$ and $\chi_c$ states. The contribution to the $J/\psi$ from $\chi_c$ is measured to be between 30% to 40%, while from $\psi'$ the contribution is from 12% to 14% [36, 37, 38]. There is no feed-down to the $\psi'$, since its mass is greater than the three lowest mass $\chi_c$'s, and all charmonia with mass greater that the $\psi'$ also have a mass greater than two D's, so would decay into open charm.

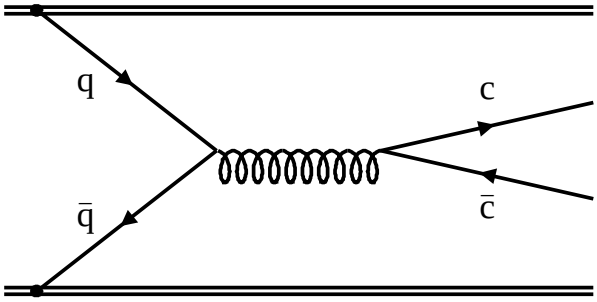


Figure 2.9: Charmonia production diagram from quark-antiquark annihilation

## 2.4 Nuclear Effects

From the results of the experiments discussed earlier and others, numerous effects have been modeled. This section will cover some of the more prominent models which explore such effects as absorption, shadowing, and energy loss.

### 2.4.1 Absorption

The main effect that has been theorized is an absorption effect. Absorption is the disassociation of the $J/\psi$, $\psi'$, or the precursor $c\bar{c}$ by the nuclear medium. It is generally thought that since the charmonia total cross-section per nucleon is reduced in heavier nuclei, absorption must be occurring. If there were no absorption, then suppression of the $J/\psi$ in one kinematic range would have to be compensated by an enhancement in the rest of the kinematic range. While the above statements are partially true, they do not take into account other effects, such as shadowing and

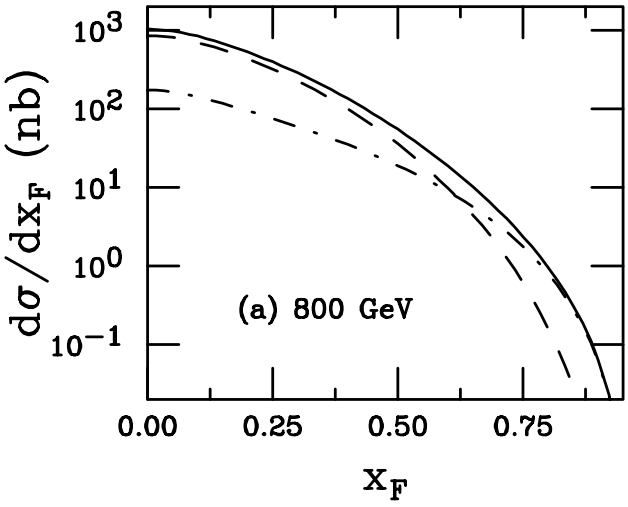


Figure 2.10: The $\psi$ $x_F$ distribution for E866. The contributions from $gg$ fusion (dashed) and $q\overline{q}$ annihilation (dot-dashed) are given along with the total (solid). [33]

initial state energy loss (discussed later), which could also reduce the total cross-section.

There are three main factors that effect absorption: the production mechanism, the formation time, and the nuclear medium. All of these factors intertwine, so are difficult to separate. As seen in the previous section, the $c\bar{c}$ may be produced in either a color singlet state or a color octet state. The color singlet state starts as a point-like particle, while the color octet is a colored state and should be of a size on the order of a gluon. Therefore, the color octet state should have a larger cross-section for interacting in the nuclear medium, and hence have a larger chance for disassociation.

The nuclear medium through which the $c\bar{c}$ or $J/\psi$ passes might cause its absorp-

tion. Of course, the parton soup that makes up the nucleus is the main instigator of absorption. However, some interaction with comovers [18] may also be possible. A comover is a secondary particle or parton moving with a velocity similar to the charmonium velocity. These particles may also interact with the charmonium causing disassociation. While comovers are prevalent in nucleus-nucleus collisions, their effect in proton-nucleus collisions may be small, but not inconsequential.

Finally, the formation time will influence the absorption by determining which medium the $c\bar{c}$ or the charmonia is passing through. The results as a function of the kinematic variable $x_F$ could be very sensitive to the formation time. For fast, or large $x_F$, $J/\psi$'s (or $\psi'$'s) will hadronize well outside the nucleus, so the only effects that should be seen are on the pre-charmonia $c\bar{c}$. This implies that there should be little difference in the suppression between the $J/\psi$ and the $\psi'$. At some value of $x_F$, for a short enough formation time, the $c\bar{c}$ will begin to hadronize in the nucleus or in a greater density of comovers. Since the $\psi'$ is larger than the $J/\psi$ and has a smaller binding energy, the $\psi'$ would have a greater chance of becoming disassociated.

Figure 2.11 [33] demonstrates some of the absorption effects for 800 GeV proton-nucleus collisions. In (a) the effects of the $c\bar{c}$ produced in a pure octet state are shown. In octet production all of the charmonia states have the same probability of being absorbed, so there is no $x_F$ dependence. Final state interactions have been ignored. In (b) pure singlet production is examined. Here the $c\bar{c}$ is produced in a

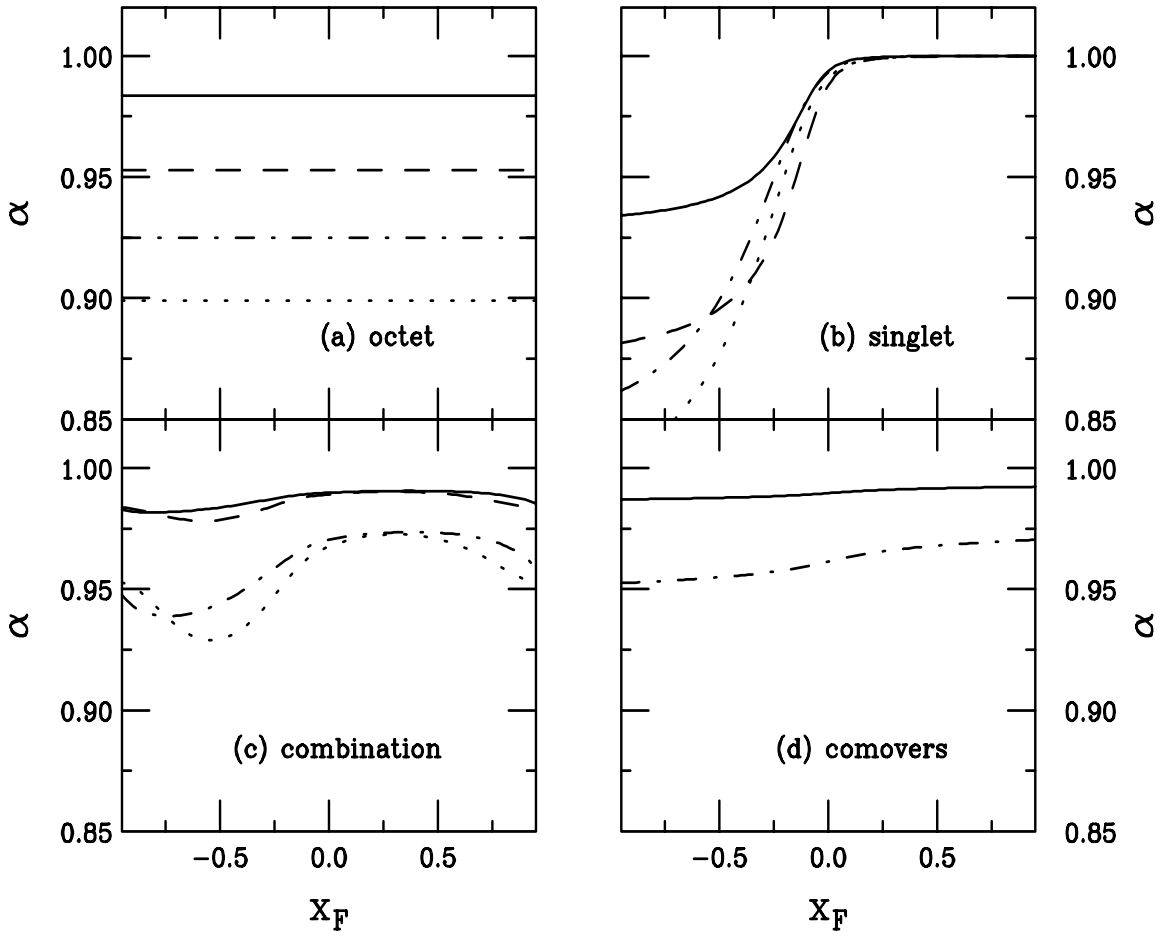


Figure 2.11: The $A$ dependence of nuclear absorption models is given in (a), (b) and (c) and the comover $A$ dependence is shown in (d). In (a), octet cross-sections of 1 mb (solid), 3 mb (dashed), 5 mb (dot-dashed) and 7 mb (dotted) are shown. Singlet absorption is shown in (b) for $\psi$ with $\sigma^{\rm s}_{\psi N} = 5$ mb (solid) and 10 mb (dashed) as well as $\psi'$ with $\sigma^{\rm s}_{\psi' N} = 15$ mb (dot-dashed) and 20 mb (dotted). A combination of octet and singlet production is assumed in (c). The curves represent: $\psi$ absorption with $\sigma^{\rm octet}_{\rm abs} = 1$ mb and $\sigma^{\rm singlet}_{\rm abs} = 1$ mb (solid) and $\sigma^{\rm octet}_{\rm abs} = 3$ mb and $\sigma^{\rm singlet}_{\rm abs} = 5$ mb (dot-dashed); $\psi'$ absorption with $\sigma^{\rm octet}_{\rm abs} = 1$ mb and $\sigma^{\rm singlet}_{\rm abs} = 3.7$ mb (dashed) and $\sigma^{\rm octet}_{\rm abs} = 3$ mb and $\sigma^{\rm singlet}_{\rm abs} = 19$ mb (dotted). In (d), comover interactions are shown for $\sigma_{\psi \rm co} = 0.67$ mb (solid) and $\sigma_{\psi' \rm co} = 3.7\sigma_{\psi \rm co}$ (dot-dashed). [33]

weakly interacting state, so there is no absorption at the larger values of $x_F$, but final state effects can be seen at the smaller $x_F$ values. These effects are due to the different size of the particles and the $J/\psi$ and $\psi'$ formation times are different. In both of these calculations the color evaporation model was used.

Figure 2.11(c) shows the calculation with singlet and octet production using the non-relativistic QCD model. Here the ratio for singlet to octet production is $x_F$ dependent. Also the dependencies of the $\chi_c$ feeding the $J/\psi$ provide some $x_F$ dependence. Finally, in (d) a calculation for comovers is studied. Here comovers are assumed to only interact with final state charmonia including the $J/\psi$'s parent $\chi_c$'s and $\psi'$.

### 2.4.2 Shadowing

Deep-inelastic scattering experiments [39, 40, 41, 42], have shown that at small $x$, where $x$ is the parton momentum fraction, there is a depletion in the nuclear structure functions for heavy nuclei as compared to light nuclei. This is commonly referred to as nuclear shadowing. In the E866 experiment a depletion of the parton distributions at small $x_{target}$, or $x_2$, would appear as a depletion at large $x_F$. From shadowing models [17], the contribution for $q\bar{q}$ annihilation can be calculated and does not show as strong an $x_F$ effect as seen in NA3 or E772. While the gluon-gluon fusion contribution is not well understood, gluon shadowing is not expected to be significantly

different from quark shadowing.

### 2.4.3 Energy Loss and Multiple Scattering

Energy loss has been the subject of theoretical interest [12, 13, 14, 15]. It could effect all phases of $J/\psi$ production, from the incoming parton to the $c\bar{c}$ pair to the final state charmonia. Since energy loss would show up as a loss in momentum for the charmonia produced in the heavier nuclei, this would shift the distribution in the larger nuclei to smaller forward momentum, or $x_F$ and thus give a suppression at larger $x_F$.

When the incident parton, the $c\bar{c}$ or the physical $J/\psi$ multiple scatters in the nucleus, it will gain transverse momentum. For a heavier nucleus, there would be more multiple scattering which would shift events to higher $p_T$ causing a depletion at small $p_T$ and an enhancement at larger $p_T$. This is the accepted explanation for the $p_T$ dependence seen in Figure 2.2. If there is an increase in multiple scattering in heavier nuclei, there should also be an increase in energy loss.

The energy loss for the incoming parton can be studied by looking at the Drell-Yan process [5]. The dilepton's small interaction cross-section allows for study of the incoming quarks. Still, while Drell-Yan production tells us about quarks, the majority of charmonia production is produced from gluons. Gavin and Milana [12] treat gluons as just a quark with a color factor of 9/4. As can be seen from the

Drell-Yan ratio in Figure 2.3, the initial state energy loss is still too small to account for the charmonia suppression.

### 2.4.4 Intrinsic Charm

The proton can be thought of as occasionally being in a Fock state such that there is an intrinsic $c\bar{c}$ (charm) in the proton [16]. If the proton is in a state such that there is intrinsic charm, these intrinsic heavy quarks would carry a large fraction of the momentum. This mechanism would be most important at large $x_F$. Essentially in the intrinsic charm model, provided the $c\bar{c}$ is in a color singlet state, it passes through the nucleus without interacting. The light valence quarks in the proton are of hadronic size and will strongly interact on the front surface of the nucleus. Since the light quarks are stripped away as a surface effect, the cross-section for intrinsic charm is expected to be proportional to $A^{2/3}$ [43].

# Chapter 3

# The Experiment

The spectrometer used by E866, shown in Figure 3.1, was located in the Fermi National Accelerator Laboratory (FNAL) Meson East beam line. This spectrometer was also employed by previous experiments (E605, E772, and E789) [2]. Many improvements to the trigger and data acquisition system were made for E866, but the spectrometer still looks much as it did in the previous experiments.

The E866 spectrometer was a forward $x_F$ dimuon spectrometer. However, by adjusting the target placement and magnet settings, the dimuon $x_F$ was adjusted from slightly less than one to a limited negative $x_F$ range. In this experiment three different spectrometer settings were used. They were named for the $x_F$ range that they covered and can be seen in Table 3.1. We will refer to these data sets by their abbreviations throughout this text.

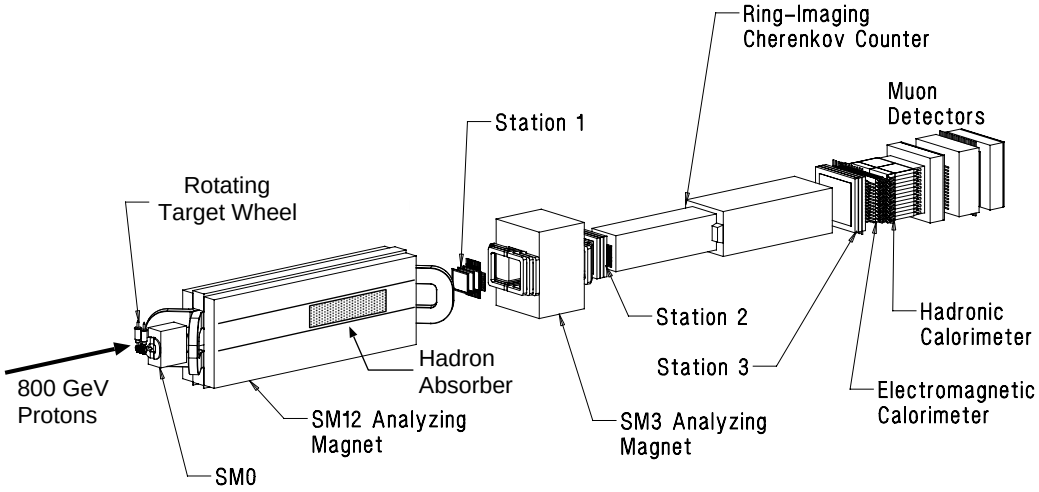


Figure 3.1: The FNAL E866/NuSea Spectrometer.

| Name | Abbreviation | $x_F$ Range |
|---|---|---|
| Small $x_F$ | SXF | $-0.15$ to 0.30 |
| Intermediate $x_F$ | IXF | 0.20 to 0.75 |
| Large $x_F$ | LXF | 0.30 to 0.95 |

Table 3.1: The data sets and the $x_F$ ranges that they cover.

We will often refer to a spectrometer-fixed coordinate system. In the right-handed E866 coordinate system, the beam protons move "downstream" in a positive direction along the Z-axis, with the origin at the upstream face of the large magnet (SM12). The Y-axis points straight up, perpendicular to the floor.

## 3.1 Meson East Beam Line

The protons for the experiment were delivered to the Meson East Beam Line from the FermiLab Tevatron [44], a one kilometer radius super-conducting proton synchrotron. During the E866 nuclear dependence runs, the Tevatron delivered approximately $2 \times 10^{13}$ protons per spill to all of the experiments, of which E866 received between $1-5 \times 10^{11}$ protons, depending on the data set. The protons were bunched and accelerated in 18.9 ns RF packets (called buckets), which were then smoothly extracted over 20 seconds. The Tevatron magnets were then ramped down for approximately 15 seconds, which, with the ramping time, makes the entire spill cycle approximately one minute. During the months of the experiment in which the $\psi$ nuclear dependence measurement was taking place, over 8800 trillion protons were received by E866.

As a proton moves down the Meson East beam line, it passed through several detectors. These detectors determined the position, size and luminosity of the beam. In the Meson East 3 (ME3) portion of the beam line, the protons passed through an

ion chamber (IC3). This was one of the two main luminosity detectors. The other was a secondary emission monitor (SEM6) located just upstream of the spectrometer in ME6. Also in ME6 were two segmented wire ion chambers (SWIC's) and the beam position monitor (BPM), which were used to record the size and position of the beam. The size of the beam at the SWIC was typically about 6 mm wide and 1 mm high (full width at half maximum).

## 3.2 Targets

After the beam has passed through the SWIC's, it reaches the ME6 target cave. The targets used in the nuclear dependence measurements were placed in a four position rotating wheel. Three solid targets were used for each data set, as shown in Table 3.2, with the fourth position left empty. The solid targets, except for beryllium, were made up of 7.28 cm diameter disks with the total thicknesses given in the table. The beryllium target was a rectangular parallelepiped which measured approximately 3 by 3 by 2 inches. The target wheels were rotated such that each target received 2 spills for every spill the empty target received for the LXF and IXF data sets. For the SXF data set each target received 4 spills for each empty. Interchanging the targets every few minutes reduced the systematic uncertainties.

The position of the target wheel relative to the spectrometer varied with data set. The Z position of the target wheel can be seen in Table 3.2. The target position for

| Data Set | Z position (in) | Target | Thickness (cm) | % int |
|---|---|---|---|---|
| LXF & IXF | -203. | Be | 7.78 | 19.1 |
| | | Fe | 2.05 | 12.2 |
| | | W | 0.899 | 9.38 |
| SXF | -24. | Be | 5.11 | 12.6 |
| | | W1 | 0.300 | 3.13 |
| | | W2 | 0.599 | 6.25 |

Table 3.2: The targets used in different data sets. The SXF data set used two thicknesses of tungsten target denoted by W1 and W2. % int is the percentage of a nuclear interaction length for that target.

the LXF data set was much farther upstream than for the SXF. We will see the need for this in the next Section.

## 3.3 Magnets and Spectrometer Settings

The two magnets just after the targets, SM0 and SM12, are used to define the acceptance of the spectrometer. The third magnet, SM3, is located farther downstream, and is used as a momentum analyzing magnet. All three magnets used in the spectrometer are dipole magnets which produce a magnetic field aligned in the X direction. This will cause charged particles moving in the Z direction to bend in the Y direction. Wherever possible, helium-filled bags were placed in the path of the muons traversing the spectrometer in order to minimize collisions between the muons and air particles.

The farthest upstream and smallest magnet, SM0, is 72 inches long and had a maximum current of 2100 Amperes generating a momentum kick of 0.94 GeV/c. SM0 mainly provided additional separation for the oppositely charged muon pairs. This helped to increase the acceptance for the lower mass pairs and other dimuons with small opening angles.

The middle magnet, SM12, is the largest of the three magnets at over 45 feet in length. When operating at the maximum current of 4000 Amperes, SM12 induces a 7.0 GeV/c transverse momentum kick to the charged particles that travel its entire length. The main purpose of this magnet is to focus the dimuons through the spectrometer. The magnetic field strength of this magnet had the greatest effect on the mass and $x_F$ acceptances in the experiment. The beam dump and hadron absorber wall are located inside SM12 as shown in Figure 3.2.

To stop any protons that did not interact with the target, a beam dump was placed 68 inches downstream of the face of SM12, and continued for 129 inches. The beam dump was made of copper and was water cooled. There was a 12 inch deep hole in the center of the front of the dump to limit the number of back-scattered particles. The beam therefore did not interact with the dump until it reaches $Z = 80$ inches. Still the beam dump was 26.5 interaction lengths thick.

The E866 spectrometer is designed to be a high rate dimuon spectrometer. To achieve the desired rates, particles other than muons must be prevented from hitting

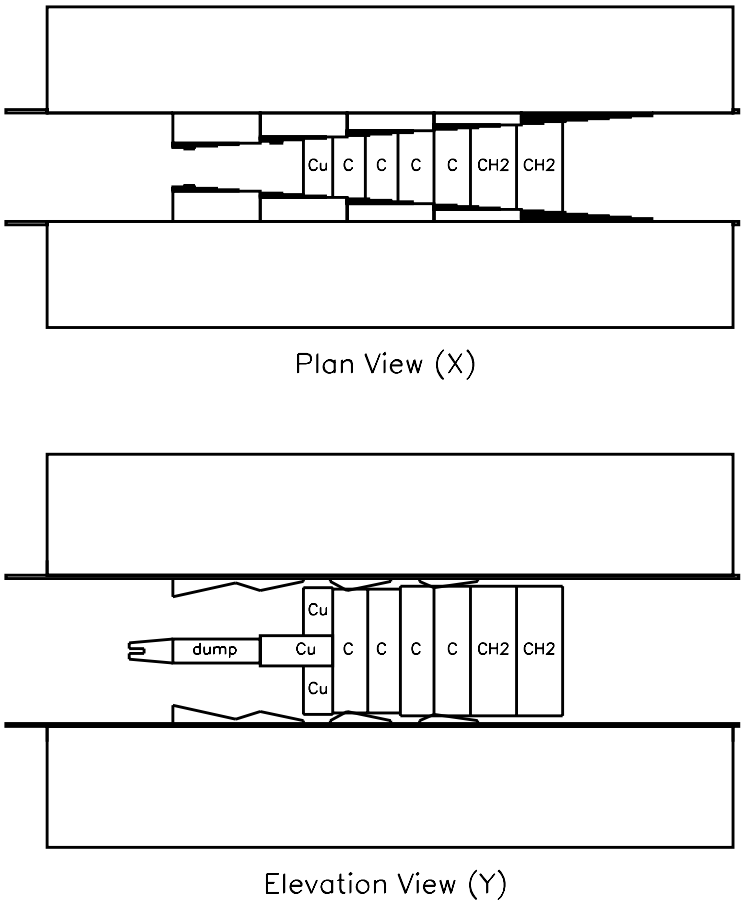


Figure 3.2: The beam dump and absorber wall inside the aperture of SM12.

the detectors. To stop these particles, a hadron absorber was placed at the downstream end of SM12 as seen in Figures 3.1 and 3.2. The absorber was seven layers thick and filled the entire X and Y aperture of the magnet. The first layer was 24 inches of copper, followed by four layers of 27-inch-thick carbon. The last two layers were each 36 inches of polyethylene doped with boron to increase the neutron absorption. The entire wall was over 13 nuclear interaction lengths thick.

The third magnet in the spectrometer, SM3, was located just after the first detector station. This magnet was used as an analyzing magnet to measure the momentum and charge of the particles when reconstructing their tracks. For all of the data sets this magnet was operated at a constant current of 4230 Amperes which provided a Y momentum kick of 0.91 GeV/c.

The magnet settings, target position, and the trigger, which will be discussed in Section 3.5, defined the acceptance for each data set. The magnet currents for each data set can be found in Table 3.3. For the LXF and SXF data sets, half of the data was taken with the currents given in Table 3.3 while the other half was taken with the polarities of all magnets reversed (not shown in the table). The IXF data set were taken over a short period of time (two days), and only one polarity was used.

| Data Set | SM0 | SM12 | SM3 |
|---|---|---|---|
| LXF | 0 | 2800 | 4230 |
| IXF | 2100 | -2800 | -4230 |
| SXF | 0 | 1420 | -4230 |

Table 3.3: The magnet currents used for each data set. The currents shown are in Amperes. Since the magnets were operated in both polarities, the sign of the current is only present to demonstrate relative polarity.

## 3.4 Detectors

There were four detector stations in the E866 spectrometer. Stations one, two, and three consist of drift chambers and hodoscopes, while station four consists of proportional tubes and hodoscopes. These stations determined the X and Y position of the charged particles as they passed through them. Given the position of a muon at each tracking station and the magnetic field strengths, the four-momentum of the muon can be determined.

As mentioned before, station one was located between SM12 and SM3. Immediately following SM3 was station two, which was followed by a ring-imaging Cherenkov detector (RICH). Since the RICH was not needed in this experiment, it was filled with helium and functioned essentially as another helium bag. Downstream of the RICH was station three. Next came an electromagnetic calorimeter and a hadronic calorimeter. These played the roles of hadron absorbers as did the walls of lead and zinc which followed them. This shielding made it unlikely that anything that reached

station four was not a muon, but to make sure there were walls of cement between the proportional tube planes in station four.

### 3.4.1 Hodoscopes

At all four stations there was a plane of scintillator hodoscopes oriented to give a coarse Y position of the particle. At stations one, three, and four there were also hodoscopes oriented to give the X position. The hodoscopes consisted of a long, thin "paddle" of plastic scintillator optically coupled to a photomultiplier via a plexiglass light guide. The entire paddle and light guide were wrapped with black electrical tape to shield the assembly from room lights. This allows the photomultiplier to detect only the light generated from a charged particle passing through the scintillator. The dimensions of the hodoscopes can be seen in Table 3.4. Note that the detector planes were named by their orientation and station location. For example, the "Y1 hodoscopes" refer to the station one plane of hodoscopes which measured the Y position of the particle. Each plane of detectors was made up of two sets of paddle-photomultiplier arrays with the ends of the paddles opposite the photomultiplier tubes touching each other in the middle of the plane. In some cases there was a small gap between the ends of two adjacent paddles. The widths of these gaps are shown in Table 3.4 as "center gap width." The half planes are referred to by appending a "u" or a "d", up or down, for the X planes, and a "l" or a "r", left or right for the Y

| Detector Plane | Number of Counters | Counter Width | Aperture (x×y) | Center Gap Width |
|---|---|---|---|---|
| Y1 | 32 | 2.50 in. | 47.50 in.×40.75 in. | 0.47 in. |
| X1 | 24 | 4.00 in. | 47.53 in.×40.78 in. | 0.38 in. |
| Y2 | 32 | 3.00 in. | 64.63 in.×48.63 in. | 0.66 in. |
| X3 | 24 | 8.68 in. | 105.2 in.×92.00 in. | 1.00 in. |
| Y3 | 26 | 7.50 in. | 104.0 in.×92.00 in. | 0.00 in. |
| Y4 | 28 | 8.00 in. | 116.0 in.×100.0 in. | 0.00 in. |
| X4 | 32 | 7.125 in. | 126.0 in.×114.0 in. | 0.00 in. |

Table 3.4: Information on hodoscopes.

planes.

Hodoscopes are fast detectors, in the sense that their response and recovery time is fast compared to other detectors. This made the hodoscopes useful for triggering in E866, which will be discussed in Section 3.5.

### 3.4.2 Drift Chambers and Proportional Tubes

At each of stations one, two and three, there were three pairs of drift chamber planes. The middle pair was oriented with the sense wires in the horizontal to measure Y position. Keeping a similar naming convention as with the hodoscopes, for station one, the upstream Y plane is called Y1 while the downstream plane is called Y1′. In each pair of wire planes, the primed plane's sense wires are offset from the unprimed plane by 1/2 of a cell size. Since the drift time does not show on which side of the wire the particle passed, correlations between the two planes will remove these

ambiguities. The construction details and operating conditions of the drift chambers can be found in Table 3.5. The other pairs are the U and V planes, with the U plane on the upstream side of the Y plane and the V downstream. These sense wires are not parallel to the Y axis so they do not measure the X position directly. Instead the wires for the U planes are tilted approximately $+14^{\circ}$ toward the Y axis, while the V planes are tilted at approximately $-14^{\circ}$. Note that $14^{\circ}$ corresponds to a slope of 0.25. The combination of any two of the U, V, or Y planes can locate a particle in X and Y.

Multiple scattering in the absorber downstream of station three reduced the need for precision in position measurement at station four. This fact, coupled with the larger size required for the detectors, led to the use of proportional detectors rather than drift chambers. The proportional tube (PT) planes were made up of two layers of 1 inch square cells. Each layer was offset by 1/2 of a cell. The dimensions of the PT planes can be seen in Table 3.5. Since there were two Y PT planes, the upstream Y PT plane is labeled PT-Y1 and the other PT-Y2. The lone X PT plane is simply labeled PT-X.

The gas for all the drift chambers and the proportional tubes was 50% argon and 50% ethane. To prevent build up on the wires the gas mixture was bubbled through ethanol before entering the chambers, which minimized sparking.

| Detector Plane | Number of Wires | Drift Cell Size | Aperture (x × y) | Operating Voltage |
|---|---|---|---|---|
| Y1 | 160 | 0.25 in. | 48 in.×40 in. | +1700 V |
| Y1′ | 160 | 0.25 in. | 48 in.×40 in. | +1700 V |
| U1 | 200 | 0.25 in. | 48 in.×40 in. | +1700 V |
| U1′ | 200 | 0.25 in. | 48 in.×40 in. | +1700 V |
| V1 | 200 | 0.25 in. | 48 in.×40 in. | +1700 V |
| V1′ | 200 | 0.25 in. | 48 in.×40 in. | +1700 V |
| Y2 | 128 | 0.40 in. | 66 in.×51.2 in. | -2000 V |
| Y2′ | 128 | 0.40 in. | 66 in.×51.2 in. | -2000 V |
| U2 | 160 | 0.388 in. | 66 in.×51.2 in. | -1950 V |
| U2′ | 160 | 0.388 in. | 66 in.×51.2 in. | -1975 V |
| V2 | 160 | 0.388 in. | 66 in.×51.2 in. | -2000 V |
| V2′ | 160 | 0.388 in. | 66 in.×51.2 in. | -2000 V |
| Y3 | 112 | 0.82 in. | 106 in.×91.8 in. | -2200 V |
| Y3′ | 112 | 0.82 in. | 106 in.×91.8 in. | -2200 V |
| U3 | 144 | 0.796 in. | 106 in.×95.5 in. | -2200 V |
| U3′ | 144 | 0.796 in. | 106 in.×95.5 in. | -2200 V |
| V3 | 144 | 0.796 in. | 106 in.×95.5 in. | -2200 V |
| V3′ | 144 | 0.796 in. | 106 in.×95.5 in. | -2150 V |
| PT-Y1 | 120 | 1.00 in. | 117 in. ×120 in. | +2500 V |
| PT-X | 135 | 1.00 in. | 135.4 in.×121.5 in. | +2500 V |
| PT-Y2 | 143 | 1.00 in. | 141.5 in.×143 in. | +2500 V |

Table 3.5: Information on the drift chambers and proportional tubes.

| Data Set | Sub-set | Physics A Trigger | Physics B Trigger | Matrix File | SM12 Current |
|---|---|---|---|---|---|
| LXF | 1 | 20 | 22 | lxfint2 | +2800 |
| | 2 | 21 | 23 | lxfint2 | +2800 |
| | 3 | 22 | 23 | lxfint2 | +2800 |
| | 4 | 21 | 24 | lxfint2 | -2800 |
| IXF | 1 | 12 | 12 | low2 | -2800 |
| SXF | 1 | 23 | 24 | sxfn5w | -1420 |
| | 2 | 23 | 24 | sxfn5w | +1420 |

Table 3.6: The triggers used for each data subset.

## 3.5 Trigger

It was the job of the trigger to decide which events to record on tape and which ones to throw away. The new trigger system implemented for E866 [7, 45] used only the hodoscopes to determine the validity of an event. For a given data set, several different triggers may have been used. It was these triggers and the polarity of the magnets that divided the data sets up into the data subsets seen in Table 3.6. The most important parts of the trigger were the trigger matrix modules and the track correlators, which are described in the following paragraphs.

The left and right signals from the Y1, Y2, and Y4 hodoscope planes were brought into trigger matrix modules. The combination of muon hodoscope hits in these three planes are used to form a "road". The trigger matrix was a look-up table of possible roads that a muon pair could travel through the hodoscope planes. This look-up table was formulated from Monte Carlo studies of $J/\psi \rightarrow \mu^+\mu^-$ events in the desired

kinematic range. Since different target Z positions would have different roads, the trigger matrix was very important in discriminating against muons from the dump. Monte Carlo analysis used to simulate muons from the dump could be used to remove cells from a matrix. Real-time analysis of a portion of the data was also used to determine which cells in a matrix fired more frequently as a result of being hit by muons from the dump. These cells could then be removed from the trigger.

There were four trigger matrices of four modules each. Each matrix covered a different hodoscope plane quadrant which was labeled either matrix-up-left (MUL), matrix-down-left (MDL), matrix-up-right (MUR), or matrix-down-right (MDR). The output of these modules were then sent to the track correlator.

There were three track correlators. The first two, Physics A and Physics B, were the physics triggers. The third was the diagnostic trigger. This trigger mainly detected cosmic rays and was used during down-time to make sure the spectrometer was operating optimally.

Physics A (PhysA) was the main trigger for the experiment. Two typical PhysA triggers are shown in Table 3.7. Each track correlator can accept four triggers. These are labeled PHYSA1 through PHYSA4 in the table. The normal trigger used in E866 is shown under trigger set A20. This trigger simply takes the outputs from the matrix modules to determine which events are kept. Since the magnet SM12 sweeps the muons either up or down depending on charge, the majority of oppositely

| Trigger Set | Trigger Name | Prescale Factor | Description |
|---|---|---|---|
| A20 | PHYSA1 | 1 | (MUL * MDR) + (MUR * MDL) |
| | PHYSA2 | 1 | (MUL * MUR) + (MDL * MDR) |
| | PHYSA3 | 1 | (MUL * MDL) |
| | PHYSA4 | 1 | (MUR * MDR) |
| A21 | PHYSA1 | 1 | (MUL * MDR * (!S4DL1 + !S4UR1)) + (MUR * MDL * (!S4DR1 + !S4UL1)) |
| | PHYSA2 | 1 | (MUL * MUR * (!S4DL1 + !S4DR1)) + (MDL * MDR * (!S4UL1 + !S4UR1)) |
| | PHYSA3 | 1 | (MUL * MDL) * (!S4UL1 + !S4DL1) |
| | PHYSA4 | 1 | (MUR * MDR) * (!S4UR1 + !S4DR1) |
| B22 | PHYSB1 | 10 | ( X134L * X134R ) |
| | PHYSB2 | 1000 | MUL + MDL + MUR + MDR |
| | PHYSB3 | - | - |
| | PHYSB4 | - | - |

Table 3.7: A description of some typical triggers used. Here a "*" represents a logical AND, a "+" represents a logical OR, and a "!" represents a logical NOT.

charged muons will be in some combination of the up and down matrices. The trigger PHYSA1 will detect the left-right oppositely charged muon pairs, while the triggers PHYSA3 and PHYSA4 will detect the left-left and right-right oppositely charged muon pairs respectively. The PHYSA2 trigger is the like-sign trigger, which detects like charged muon pairs. As will be seen in the next chapter, these pairs will be useful in removing random muon pairs from the data.

Also seen in Table 3.7 is the trigger set A21. This trigger is very similar to A20, except that here some vetos are also included from the station four X and Y hodoscopes. These were designed to reduce the contribution of muons from the beam

dump.

The study trigger shown in Table 3.7 is B22. The only difference between this PhysB trigger and most other PhysB triggers used in the nuclear dependence data sets was the prescale factor. Using a prescale factor of N means that every Nth time the trigger was satisfied the event would be recorded. The B1 trigger shown in the table recorded the coincident muon pairs that passed on the left and right sides of the spectrometer as measured by the X1, X3 and X4 hodoscopes. For this experiment, the B1 trigger was mainly activated from dimuons coming from the dump. The B2 trigger accepted single muons. These muons are useful for predicting the number of random muon pairs in the data, as will be seen in Section 4.5.1.

The IXF trigger was similar to the other triggers, except for two differences. The major difference was that the IXF trigger was not set up to accept single muons. The other difference was that the like sign trigger, PHYSA2, was prescaled by four. Together these differences make it more difficult to predict the random muon pairs, as will be seen.

## 3.6 Data Acquisition System

The Data Acquisition System (DAQ) for E866 was an upgraded version of the system used for E789. While the readout system was essentially the same, the Versa Module Eurocard (VME) based control and archiving system was much improved.

Once the trigger had been satisfied the system busy signal would be set, which would inhibit further triggers. The transport system then read out all of the coincidence registers from the hodoscopes and proportional tubes, the time-to-digital converters from the drift chambers, and other information sent out by the trigger and other sources. All of this information was then sent to a pair of high speed memory boards.

At the end of each spill, a large amount of spill information was also recorded. This included information about which target was being used, magnet currents, the beam position and intensity, and other information important to the experiment.

During the twenty seconds of the spill when the beam was being delivered, the data were copied to a pair of high speed memory boards. Once one of the high speed memory boards was full it would be drained to a large memory buffer while the other memory board was being filled. During the next forty seconds, the data were formatted and sent down the VME pipeline. The data were then sent to the taping system where the data were recorded onto Exabyte tapes. All of the spill information and a fraction of the data was sent to the online monitoring system. This system displayed a variety of information which allowed the shift chief to observe any problems that might occur. The data that were sent would be analyzed in real time, to ensure that the experiment was running smoothly.

Once a data tape was produced from the data acquisition system (DAQ), the tape

was then copied. The copies were carried to the FermiLab computing center on a regular basis to be stored in their tape vault.

# Chapter 4

# Analysis

Once the raw data tapes have been gathered, the data have to be processed to remove the unwanted events and have to be converted into a more easily accessible form. These data are then presented to demonstrate the dependence on the desired kinematic variables. This chapter will detail this process.

## 4.1 Data Sets

The data sets are reviewed here since they will be discussed in detail in this chapter. Due to the differences in the data sets they must each be analyzed in a slightly different method.

The main distinction between the data sets is the spectrometer's $x_F$ setting, which was controlled by the magnet settings, target placement and the trigger. It is the

| $x_F$ | Subset | Matrix | Trigger | Magnet | Size |
|---|---|---|---|---|---|
| | 1 | lxfint2 | 20 | 0/ 2800 | 7.4 |
| LXF | 2 | lxfint2 | 21 | 0/ 2800 | 7.7 |
| | 3 | lxfint2 | 22 | 0/ 2800 | 8.1 |
| | 4 | lxfint2 | 21 | 0/-2800 | 36.3 |
| IXF | 1 | low2 | 12 | 2100/-2800 | 4.3 |
| SXF | 1 | sxfn5w | 23 | 0/-1420 | 10.3 |
| | 2 | sxfn5w | 23 | 0/ 1420 | 8.5 |

Table 4.1: The final list of data subsets that is used. The matrix column shows the name of the trigger matrix that was used for that subset, while trigger refers to the number of the PHYSA trigger. The magnet column gives the currents of the SM0/SM12 magnets and their relative polarity. The size of the data subsets is expressed in integrated intensity with the units given in $10^{14}$ protons.

trigger and the magnet settings which then divide the data into subsets as shown in Table 4.1. Unacceptable subsets or subsets used solely for testing purposes are not shown in the table.

## 4.2 First Pass

The first pass analysis used the FermiLab IBM parallel UNIX farms. E866 used several farm systems. These farms could access the copies of the data tapes in the FermiLab tape vault. The first pass analysis uses essentially the same code which was used in experiment E605. There have been many upgrades of the code since then, but the core method is still the same. The purpose of the first pass is to weed out the uninteresting events from the rest of the data. The first pass removed more

than 99.5% of the events. The remaining events were written to data summary tapes (DSTs).

The farm system copied the data from tape to a staging disk. Whenever data from a new run were encountered, all CPU nodes in the farm were then initialized for that run. This would insure that all of the settings such as magnet polarities, magnet maps, trigger and trigger matrix, and target position, were set up properly. Groups of events were then distributed to each node in the farm for reconstruction of events.

Reconstruction is the process of taking all hits that were found in the hodoscopes, the proportional tubes, and the drift chambers and determining if they could make up the tracks of a dimuon and then calculating the kinematics of that event. This process starts by looking at station two and station three drift chambers for possible muon hits. A hit in station two is found if four of the six wire chamber planes detected a particle at a given point. The hits must also match up with the hodoscope hits which actually triggered the event. Likewise hits are located in station three. The hits between stations two and three are then combined to form possible track segments.

The track segments are then extended to the other stations to verify if they are valid. Each segment is projected first through the SM3 magnet to station one to see if a valid hit (four of six planes again) is located in a given range for the various possible muon momenta. This track segment is discarded if a hit is not found. Otherwise,

the track segment is further extended to station four. At station four there must be a signal in three of five of the detector planes along the path of the track to validate the track segment.

Once the track segment extends from station one to station four, the charge and the momentum of the particle associated to this track are known. All track segments are then extended through SM12 to the target. A single bend plane approximation method is used to take into account the multiple scattering. For the first pass the muons were traced through the SM12 magnet in relatively large steps of 18 inches. The energy lost by the muons as they passed through the absorber was added back in during this process.

Events with at least two tracks were kept. Valid tracks were then combined to form dimuon pairs, and the kinematics of the event were calculated.

Since the magnet maps used in the analysis are approximations to the actual magnetic field, the analysis must be adjusted accordingly. This is done by introducing two parameters, tweek and Y0. The tweek parameter is used to adjust the magnitude of the magnetic field. While normally this is just a small adjustment, sometimes a large tweek is used to adjust the magnetic field if an appropriate magnet map is not available, as will be seen in the next section. Y0 is a vertical target offset. This offset adjusts mainly for differences between the Y position of the the beam on the target and the Y = 0 plane in the spectrometers coordinate system. Y0 also adjusts for the

| $x_F$ | Magnet | Magnet map | Tweek | Y0 |
|---|---|---|---|---|
| LXF | 0/ 2800 | bx0_2800_18.bin | 0.988 | -.5341 |
| IXF | 2100/-2800 | bx2100_m2800_18.bin | 1.0015 | -.3538 |
| SXF | 0/ 1420 | bx0_2800_18.bin | 0.510 | -.5341 |

Table 4.2: The first pass magnet maps and the tweeks used.

slight change in beam position for the various data sets.

## Differences in the First Pass

The first pass analysis for the SXF and the IXF data sets were very similar to the LXF. The SXF and the IXF used the same code as the LXF except that the minimum dimuon mass was reduced from 2.0 GeV/$c^2$ to 1.0 GeV/$c^2$ and the minimum single muon momentum was reduced from 25. GeV/c to 10. GeV/c.

Changes were made in the analysis to reflect the different settings used for each data set. For example, each data set used the magnet maps appropriate for its magnet setting. The tweeks and Y0 positions were tuned to the values shown in Table 4.2 for each data set. For the LXF and the IXF data sets, the target position, -203 inches, and multiple scattering plane, 200 inches, were the same, but the SXF data set used a target position of -24 inches and a multiple scattering plane of 525 inches.

The main difference between the SXF and the IXF or LXF was that the SXF used a one inch dump cut. This means that when the analysis program was tracing the tracks back through the magnet SM12, as it passed Z locations in the dump of 68,

104, 176, and 236 inches, the track was cut if it had a relative Y position of within one inch of the center of the dump.

## 4.3 Second Pass

Once the first pass analysis has removed the obviously bad events from the data, the second pass is performed. The second pass analysis is a refined version of the first pass which will more accurately identify the paths of the muon tracks.

In order to more accurately trace the muons back to the target, there are many refinements made in the second pass analysis compared to the first. First, two inch magnetic field maps for SM12 are used instead of the 18 inch maps of the first pass. There is also some horizontal focusing in the magnet SM12, so a Y field map is also added in this pass. The multiple scattering bend plane approximation is improved to take into account the fraction of the beam dump traversed by the muons. The energy loss calculations used in tracking the muons through the absorber were refined. A correction for the incoming beam angle was also added as well as some other minor corrections.

The results from the second pass were stored as ntuples [46]. The ntuple file is essentially a large database file which has an entry for each dimuon event. Each event entry then contains all of the information that is needed; e.g. mass, transverse momentum, target position and much more.

## 4.4 Third Pass

The third pass consisted of a careful study of the ntuple events. There were still some events that were dimuons generated in the dump or in one of the upstream beam windows. The purpose of this pass was to weed out these "bad" events. This was done using a program which selected events on the basis of ntuple cuts. The cuts used depended on the data set.

The events to be removed first were those that did not pass the spill cuts. These are events for spills that for some reason the entire spill was unacceptable. The first set of spills that were removed were those that did not have the correct run number for the data set or subset that was being studied. At times during the experiment, the target wheel would stop rotating. Since these spills may be subject to normalization problems, they were also removed. Spills for which the target did not stay in the beam for the entire spill or where the target wheel was in between targets were cut. The intensity monitors, ic3 and sem6, were inconsistent with each other at very small intensities, so any spill with an ic3 value in this range was also removed.

This pass also kept track of the luminosity of all of the good spills that survived the spill cuts. In the ntuple there are special events which mark spill entries. It is from these events that the integrated luminosity was calculated.

Events in good spills were then subjected to individual event cuts. For the LXF data set these cuts were relatively simple. The main cuts are target position cuts.

The Z value where the uniterated (prior to the multiple scattering correction) muon tracks had their closest approach near the target (called ZUNIN) had to be within 160 inches of the target. The X and Y positions at the target for both muons had to be less than 1.5 inches.

In the second pass each muon track in an event was tested to see what triggers it satisfied. In this pass those triggers were checked to make sure that they matched a valid trigger. The trigger also had to match the trigger that caused the event to be accepted. If these two trigger conditions were not satisfied, then the event was thrown out.

It was also discovered that by studying the Y positions of the tracks at Z = 86 in. (Y86) verses other variables, a large number of tracks produced in the beam dump populated around certain Y positions. The events within a 0.25 inch radius of these positions were also removed. Finally, events with $cos(\theta) > 0.6$ were cut due to the excess of random uncorrelated tracks in this region.

By the time the IXF and SXF data sets were taken the target wheel controls had been improved, so there were far fewer stuck target or moving target spills that had to be removed from the data set. The low intensity spill cut still remained. For the IXF data set the individual event cuts were fairly similar. Instead of the X and Y positions a radial cut at the target was used where the radius was less than 2.12 inches for either muon. Since the IXF data did not pass as close to the dump as did the

LXF, the Y86 cuts used were broader and just insured that the tracks passed above or below the dump. In order to ensure that the tracks stayed inside the aperture of the spectrometer, a maximum angle cut at the target was used. Events for which the momentum of the two muons was greater than the incoming proton momentum and for which the transverse momentum was greater than 6 GeV/c were also rejected. Finally, as will be shown in Section 4.5.1, the IXF data set had to be restricted to the Left Right (LR) dimuons as given by the PhysA1 trigger. Those pairs of muons where both muons pass on either the left side or on the right side of the spectrometer, which are given by the PhysA3 and the PhysA4 triggers respectively, are cut.

For the SXF data set, individual event cuts were similar to those described above. Since the target was closer to the dump, a smaller and more asymmetric ZUNIN cut was used, while a larger radius cut at the target was applied. Since the dimuons were lower in momentum than the LXF data set, the total momentum cut was lowered and the transverse momentum was lowered to 5 GeV/c. The SXF data set already had a dump cut in the first and second pass analysis, but in the second pass analysis the position of the dump was adjusted slightly. This and the adjusted multiple scattering caused some tracks to pass in regions of the dump that were not allowed in the first pass analysis. These regions were also cut out.

Once the event has passed all of the cuts, it is then stored in histograms. The histograms versus mass for each of the data sets are shown in Figure 4.1. The upper

curve in the histograms is the lineshape for the unlike-sign muons, which are the muons with opposite signs. The like-sign muons are shown by the lower curve. They will be useful in determining the random content of the unlike-sign muons, as will be discussed in Section 4.5.1.

Since results are more interesting when plotted over a range instead of integrated into a single point, the histograms in Figure 4.1 are separated into many histograms, normally by some kinematic variable that is being studied, such as $x_F$. Each of these histograms are also separated by other variables such as the target composition; furthermore the like-sign muons are separated from the unlike-sign muons. For now, the data subsets are also placed in separate histograms. This will be discussed in detail later in this chapter. The empty target provides a gauge of the dimuons that are not generated in the target. So finally, the histogram for the empty target, normalized by the integrated proton luminosity, is subtracted from the histogram for each target .

## 4.5 Counting Mesons

Once histograms of counts as a function of mass were created, the number of $J/\psi$ and $\psi'$ events could be determined by fitting the histograms with a combination of Gaussians for the meson peaks and exponentials for the background. However, it was found that, while this was adequate for the $J/\psi$'s, reliable fits to the $\psi'$'s

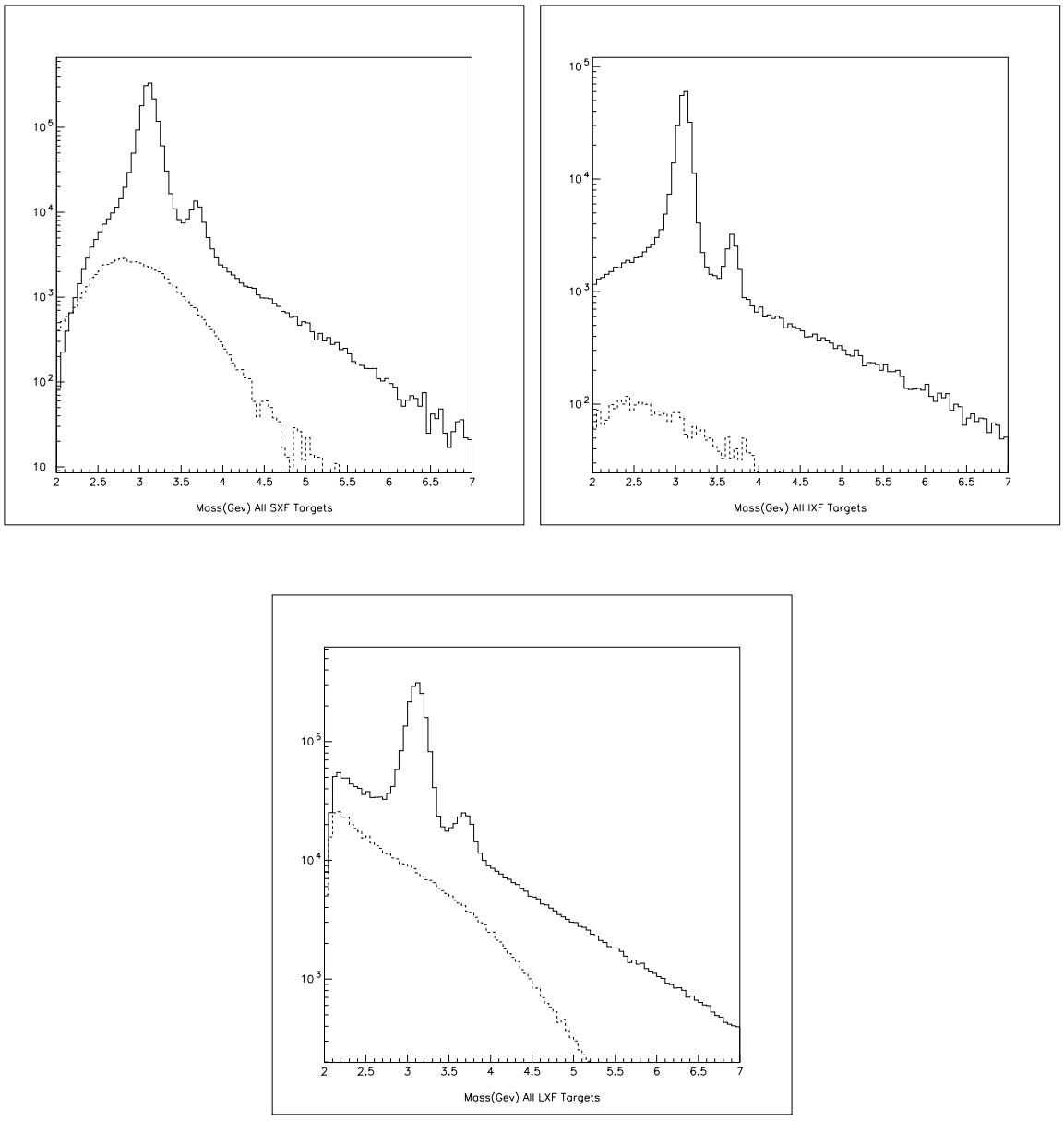


Figure 4.1: Histograms for all data in the various data sets. The solid lines are for the unlike-sign data while the dashed lines are for the like-sign data. See text for details.

could be obtained only after the fitting procedure was modified using the HMCMLL routine from the CERN HBOOK [47] library. This new procedure will take Monte Carlo distributions and fit them to the data distributions using a binned maximum likelihood fit which includes the effect of both data and Monte Carlo statistics. In order to use HMCMLL the various lineshapes that together make up the data have to be generated.

### 4.5.1 Randoms

One of the major contributions to the background is the randoms. Randoms come from unrelated muons which form accidental coincident pairs that look like dimuons originating from the target. In order to find the amount of randoms in the background, a random only data set needs to be generated.

The random data set was generated based on the "PhysB" study trigger (Section 3.5) which collected single muons. These muons can be mixed together to form pairs of muons, which can then be analyzed and placed into histograms as for the data. As with the data the randoms are also placed in separate histograms following the same procedure used with the data. Since these muons were also randomly put together, then the lineshapes of these randoms should be similar to the lineshapes of the randoms in the data. The remaining problem is to find out the normalization.

Assuming the lineshapes for the generated randoms are correct, the HMCMLL

program could just fit the randoms similar to what it does with simulated Monte Carlo shapes. This, however, is not necessary, since randoms appear in the data as both unlike-sign and like-sign dimuon pairs. The single muons can also be combined to form unlike-sign and like-sign pairs. These like-sign muons in the data are purely randoms. Therefore the like-sign muons from the singles can be fit to the like-sign muons from the data to obtain a normalization which can also be used for the unlike-sign randoms. Comparing the shapes of the like-sign randoms also provides a check to the accuracy of the generated randoms. As shown in Figure 4.2, the shapes of the two like-sign curves are very similar.

The IXF data set, however, did not have a single muon trigger. This necessitated a slightly different approach to generate randoms for this set. Since the like sign dimuons from the data are randoms, they are separated into single muons. Then they are mixed and recombined to form a set of randoms. This set is then used in the same manner as the randoms generated from single muons. Because the randoms for the IXF were generated from single muons that were gathered with a Left Right (LR) trigger, they are only able to mimic the randoms from a LR trigger. Therefore, the IXF data set was restricted to the LR trigger.

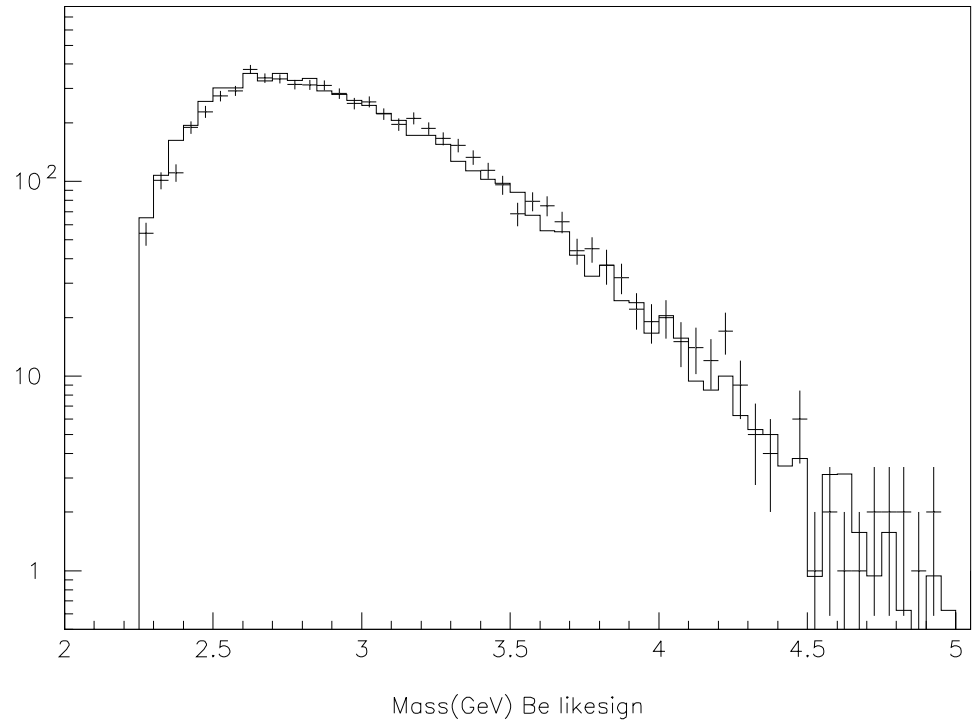


Figure 4.2: Random mass spectrum for the like-sign dimuons for the beryllium target of the SXF bin, $0.00 < x_F < 0.05$. The points are the like-sign dimuons that have passed all of the cuts given in counts per 50 MeV, as extracted from the data. The line is the fitted histogram of like-sign dimuons generated from the single muons.

### 4.5.2 Monte Carlo

The other contributors to the dimuon mass spectra are the $J/\psi$ and $\psi'$ resonance peaks and the Drell-Yan continuum. These can all be generated from the E866 Monte Carlo generator. One of the difficulties with generating Monte Carlo events is that Monte Carlo data are needed for each data subset.

The most time consuming data set for which to generate Monte Carlo could have been the LXF data set. As was seen in Table 4.1, the LXF data set was made up of several different triggers. The Monte Carlo takes into account the trigger to generate dimuons, which would imply that a different Monte Carlo would need to be generated for each trigger. Since Monte Carlo generation is very time consuming, it is preferable to run a single Monte Carlo for multiple data subsets. This was performed for the LXF by taking all of the triggers and generating the "loosest" one, essentially an "OR" of the other triggers. Then using this loose trigger a large number of Monte Carlo events were generated. The Monte Carlo then stores the data in a file in the exact same format as the data acquisition system stores the data on tape. The IXF and SXF data sets only had one trigger setting, so only one set of Monte Carlo events were generated.

The Monte Carlo generated file is then analyzed using the same method as for the data, except that it is analyzed multiple times, once for each trigger. This will then generate histogram files for each type of dimuon thrown and each type of trigger

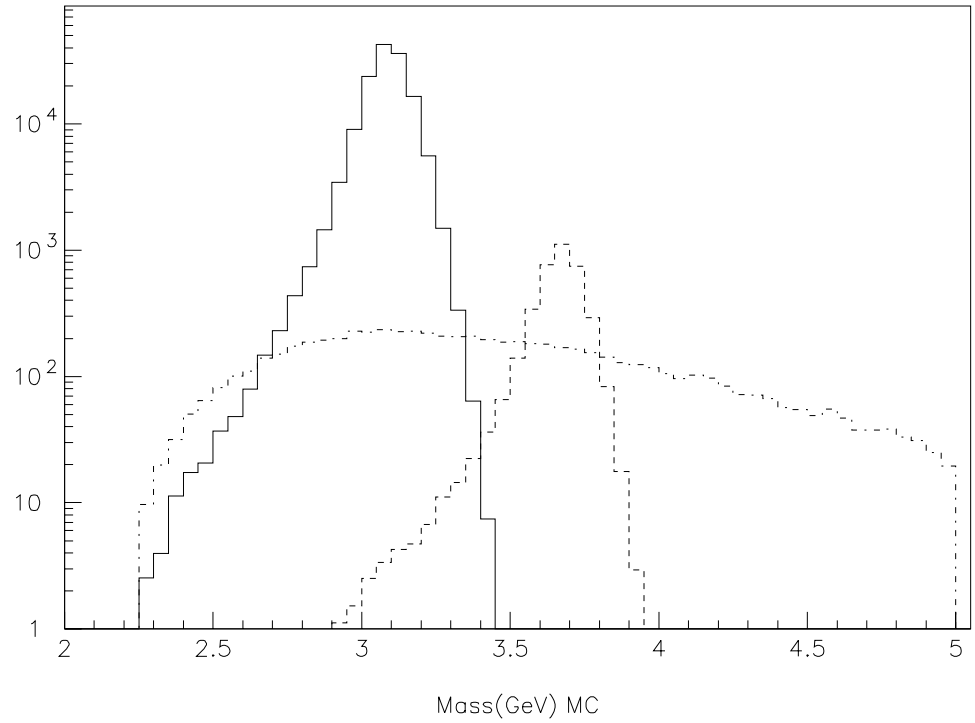


Figure 4.3: Mass spectra for the generated Monte Carlo for the SXF bin, $0.00 < x_F < 0.05$. The solid curve is for the $J/\psi$, the dashed curve is $\psi'$, while the dot-dashed curve is the generated Drell-Yan.

used. The results for the three types of thrown dimuons can be seen in Figure 4.3. The lineshapes shown in Figure 4.3 have been weighted by the values shown in Table 4.3. The weights used are the same as those when the Monte Carlo is fit (see the next section) to the data, so the total number of counts shown in the table represents the number of dimuons in the data of that type.

| | Weight | Total Counts |
|---|---|---|
| $J/\psi$ | 3.108 | 142515.3 |
| $\psi'$ | 0.0698 | 3673.5 |
| Drell-Yan | 0.2966 | 6339.2 |

Table 4.3: The weight used and the total number of counts under the Monte Carlo lineshapes shown in Figure 4.3.

### 4.5.3 Fitting

After all of the shapes that will make up the mass spectra have been generated, the HMCMLL program can be used to fit those shapes to the data. However, before the fitting can be done, all of the data subsets need to be combined.

In order to combine the data sets, the program first reads in the like-sign and unlike-sign histograms from the data; the $J/\psi$, $\psi'$, and Drell-Yan Monte Carlo data; and the like-sign and unlike-sign random pairs as generated from the singles for the first data subset. It was found that the meson shapes generated by the Monte Carlo were slightly narrow and slightly shifted in mass from the data. These were examined on a bin-by-bin basis and, if necessary, a small mass shift would be added and/or slightly wider meson peaks would be used. Since the Drell-Yan Monte Carlo did not include shadowing when generating the events, an adjustment to the Drell-Yan to account for shadowing was made. The like-sign randoms were then fit to the like-sign data, to get the normalization factor for that data subset. This was done for each

data subset.

Once all of the data subsets have been read in, they are ready to be combined. The unlike-sign data subsets are simply added to each other, as are the like-sign. Each set of Monte Carlo data is combined where each data subset is weighted by the fraction of the integrated number of protons adjusted by the livetime of the data acquisition system as compared to the total adjusted integrated number of protons for the data set. Finally, the unlike-sign random pairs are added together with each data subset weighted by the normalization factor determined previously. The like-sign random pairs are also combined.

The HMCMLL program is now used to fit the lineshapes to the data. Ideally, HMCMLL would only fit the three Monte Carlo lineshapes to the data, while the randoms remain fixed from the normalization obtained earlier. A better fit is obtained if the randoms are allowed to be fit as well. The randoms for the SXF and LXF data sets are allowed to change from their normalized value by up to 10%. The IXF randoms are allowed to vary by an even greater amount. HMCMLL will fit the given Monte Carlo and random distributions to the data distributions using a binned maximum likelihood fit which includes the effect of both data and Monte Carlo statistics. HMCMLL returns the best estimate of the fraction of each Monte Carlo distribution with an error estimate.

An example of one such fit can be seen in Figure 4.4. The solid line represents

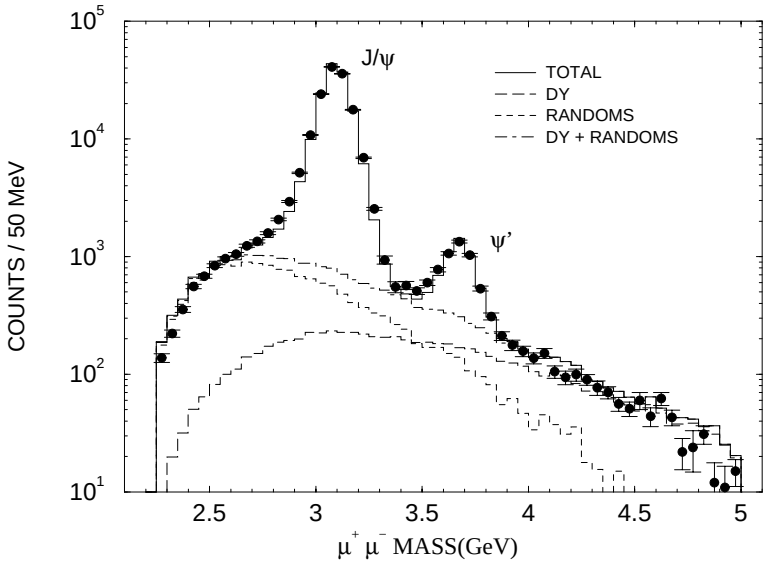


Figure 4.4: The fit for the SXF bin $0.00 < x_F < 0.05$.

the fit, and includes the random contribution and the fitted $J/\psi$, $\psi'$, and Drell-Yan contributions. The peaks for the $J/\psi$ and $\psi'$ are labeled, but the actual lineshapes for the resonances are not shown. The long dashed line, and the lowest line under the $J/\psi$ peak is the Drell-Yan, and the dashed line above it is the randoms. These combine to form the background, shown as the dot-dashed line.

It has been suggested that the fits need to include a lineshape for open charm as NA50 [21] does. Monte Carlo studies show the acceptance for open charm would be largest in the SXF data set, but still is minimal. All of the fits appear to be very good without including open charm.

## 4.6 Finding ratios and $\alpha$'s

As shown in Section 2.1.2, There are two methods for presenting the nuclear dependence of $J/\psi$ and $\psi'$ production. The first method is to give ratios of the cross-sections for two nuclei. The second method is to show the results in terms of $\alpha$ which is defined as:

$$\sigma_{pA} = A^{\alpha}\,\sigma_{pN} \tag{4.1}$$

where $\sigma_{pA}$ is the proton-nucleus cross-section, $A$ is the atomic mass of the nucleus, and $\sigma_{pN}$ is the proton-nucleon cross-section. So as can be seen from Equation 4.1, alpha is related to the cross-section ratio. Both methods will be presented here.

### 4.6.1 Cross-sections

The cross-sections for the different targets must be found. Since ratios and $\alpha$'s are being measured, fully normalized cross-section are not required. Instead, pseudo cross-sections are calculated for each target, i, and each kinematic bin, j, which are defined by:

$$\sigma_{ij} = \frac{N_{ij}}{\rho_i \cdot t_i \cdot I_i \cdot a_i} \tag{4.2}$$

where $N_{ij}$ is the number of dimuons for the target, i, and bin, j, $\rho_i$ is the target density, $t_i$ is the target thickness, $I_i$ is proportional to the total number of incident protons for that target and was found by integrating the counts from the secondary emission monitor during binning, and $a_i$ is the beam attenuation in the target. The common factors between the targets that would go into an absolute cross-section but would cancel out in the ratio are not included. This assumes that acceptance is independent of target.

It is important to note that this pseudo cross-section is the cross-section per nucleon. The total cross-section is a cross-section per nucleus and would require the cross-section per nucleon to be divided by a factor of $N_A/A_i$ where $N_A$ is Avagadro's Number and $A_i$ is the atomic mass. The reason for calculating the cross-section per nucleon is that in the absence of nuclear effects the ratio of the cross-sections per nucleon for two different targets is expected to be one. Since $\alpha$ is defined with the total cross-section, the definition for alpha with $\sigma_{pA}$ and $\sigma_{pN}$ redefined to be cross-sections per nucleon would become:

$$\sigma_{pA} = A^{\alpha-1}\,\sigma_{pN} \tag{4.3}$$

### 4.6.2 Ratios

Once the cross-sections have been calculated, the cross-section ratios are obvious to calculate. For the LXF and the IXF data sets the ratios are calculated for each of the two heavier targets by dividing their cross-section against the beryllium target.

For the SXF data set, there were only two different types of targets, a beryllium and two tungsten targets. The two tungsten targets provide an important check of the cross-section calculations, since the ratio of the two tungsten targets is expected to be one if the pseudo cross-sections were calculated correctly (see Figure 4.5). The two targets also provide a method for insuring that effects that may be due to target thickness, such as secondary production, are negligible in the ratio. The two tungsten cross-sections are then combined via weighting their errors, using the formula:

$$\sigma_W = \frac{\sigma_{W1}/\mathrm{d}\sigma^2_{W1} + \sigma_{W2}/\mathrm{d}\sigma^2_{W2}}{1/\mathrm{d}\sigma^2_{W1} + 1/\mathrm{d}\sigma^2_{W2}} \tag{4.4}$$

It is this combined tungsten cross-section that is used to calculate the ratio.

### 4.6.3 Alphas

One of the disadvantages of ratios is that they only allow two cross-sections to be displayed at one time. The parameter $\alpha$, on the other hand, allows the relationships of multiple nuclear targets to be shown. If the relationship in Equation 4.3 is assumed

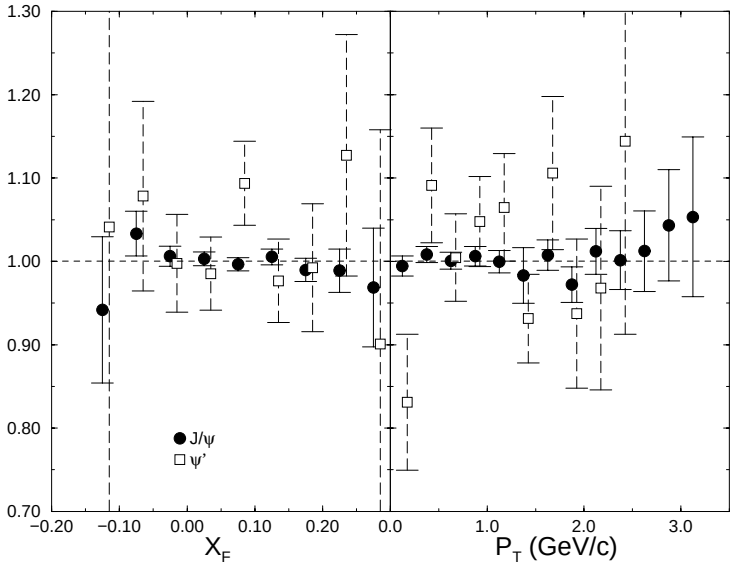


Figure 4.5: The ratio of the cross-sections of the W2 target over the W1 target for the SXF data set shown versus $x_F$ and $p_T$. The ratios for the $\psi'$, the squares, have been offset from the $J/\psi$, the circles, by 0.01 in $x_F$ and 0.05 GeV/c in $p_T$ for clarity.

appropriate, it can be rewritten after taking the log of both sides as:

$$\log(\sigma_{pA}) = (\alpha - 1) \cdot \log(A) + \log(\sigma_{pN}). \tag{4.5}$$

This is obviously a line with the slope equal to $(\alpha - 1)$.

Since the LXF and IXF data sets have three targets, Equation 4.5 is used to determine $\alpha$. The log of the cross-sections versus the log of the atomic mass is placed into a histogram, and PAW [46] is then used to fit the points to a line. The slope is then used to calculate alpha. A typical fit for each data set is shown in Figure 4.6.

The SXF data set is easier to fit, since there are only two types of targets. Here $\alpha$ is just:

$$\alpha = 1 + \frac{\log(\frac{\sigma_W}{\sigma_{Be}})}{\log(\frac{A_W}{A_{Be}})} \tag{4.6}$$

which is easily calculated. Similar results are obtained when $\alpha$ is calculated using the tungsten and beryllium targets and Equation 4.6 for the LXF and IXF data sets as when fitting using all three targets.

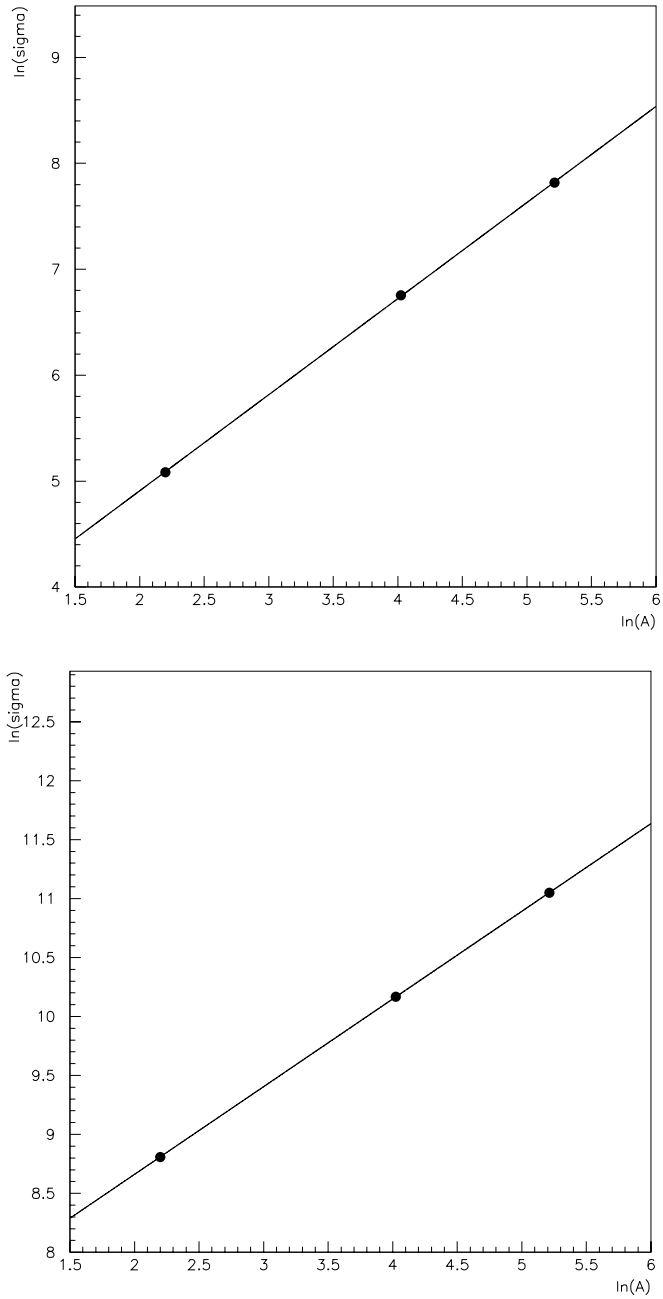


Figure 4.6: The upper plot shows a typical fit to determine $\alpha$ for the IXF data set. This is the $0.25 < x_F < 0.30$ bin. The y-axis shows the $\ln(\sigma_{pA})$ while the x-axis ln(A). The line shows the linear fit for the three points. The points are displayed larger than their error bars. The lower plot is for $0.75 < x_F < 0.80$, a typical LXF bin.

# Chapter 5

# Results

In this chapter the resulting ratios and $\alpha$'s will be presented. A correction to account for $p_T$ acceptance effects will then be used to obtain the final results. Finally, these results will be interpreted with respect to the nuclear effects discussed in Chapter 2.

## 5.1 Raw Results

Using the methods described in the previous chapter, $\alpha$ can now be plotted for the desired kinematic variable. Figures 5.1 and 5.2 show $\alpha$ versus $x_F$ and $p_T$ respectively for $J/\psi$ production. Both plots show all three data sets. The cross-section per nucleon ratios along with their respective $\alpha$ for $J/\psi$ production for each data set can be found in Table 5.1. Likewise, Table 5.2 shows the same results for $\psi'$ production.

In Table 5.1 the mean $x_F$, $\langle x_F \rangle$, is shown. For the rest of this chapter, most of the

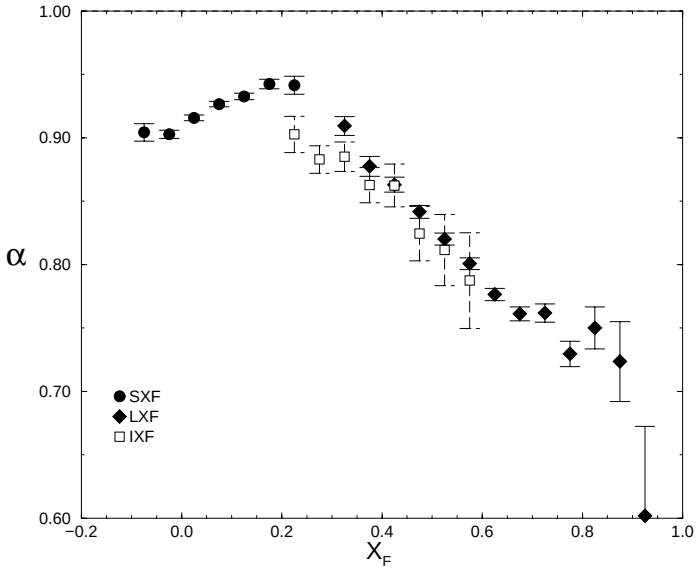


Figure 5.1: $\alpha$ versus $x_F$ for $J/\psi$ production for the three data sets.

figures and tables will refer to the mean values of kinematic variables. These mean values were determined from a Monte Carlo study, and they equal the mean value of the thrown kinematic variable for the given bin. So in Table 5.1, $\langle x_F \rangle$ is the mean thrown $x_F$ in that $x_F$ bin.

The $x_F$ plot, Figure 5.1, still shows some disagreement between the data sets. While the SXF data set and the LXF data set seem to be more consistent, the IXF data set does not appear to fill in the gap well. The $p_T$ plot, Figure 5.2, shows that the IXF data do not have the same coverage as the other two data sets. This reduction in $p_T$ coverage is an artifact of the LR trigger cut in the IXF data set. If the other dimuon triggers were able to be included, the IXF data set would also have $p_T$ coverage out to 4.0 GeV/c. The plot versus $p_T$ also shows a strong $p_T$ dependence

| SXF | | | |
|---|---|---|---|
| $\langle x_F \rangle$ | | $\sigma_W/\sigma_{Be}$ | $\alpha$ |
| -.065 | | .7494 ± .0156 | .9043 ± .0069 |
| -.019 | | .7459 ± .0073 | .9028 ± .0033 |
| .027 | | .7756 ± .0053 | .9158 ± .0023 |
| .075 | | .8017 ± .0053 | .9267 ± .0022 |
| .124 | | .8162 ± .0064 | .9327 ± .0026 |
| .173 | | .8408 ± .0096 | .9425 ± .0038 |
| .221 | | .8384 ± .0179 | .9415 ± .0071 |
| IXF | | | |
| $\langle x_F \rangle$ | $\sigma_{Fe}/\sigma_{Be}$ | $\sigma_W/\sigma_{Be}$ | $\alpha$ |
| .231 | .8451 ± .0372 | .7446 ± .0322 | .9028 ± .0143 |
| .277 | .8244 ± .0269 | .6999 ± .0229 | .8829 ± .0108 |
| .327 | .8592 ± .0299 | .7001 ± .0246 | .8851 ± .0115 |
| .377 | .7805 ± .0325 | .6604 ± .0278 | .8627 ± .0138 |
| .428 | .7975 ± .0403 | .6572 ± .0337 | .8624 ± .0168 |
| .479 | .7726 ± .0488 | .5803 ± .0382 | .8245 ± .0215 |
| .529 | .7506 ± .0615 | .5572 ± .0481 | .8115 ± .0280 |
| .581 | .6960 ± .0767 | .5224 ± .0612 | .7874 ± .0378 |
| .629 | .5832 ± .0870 | .5830 ± .0887 | .8041 ± .0492 |
| LXF | | | |
| $\langle x_F \rangle$ | $\sigma_{Fe}/\sigma_{Be}$ | $\sigma_W/\sigma_{Be}$ | $\alpha$ |
| .335 | .8511 ± .0219 | .7588 ± .0196 | .9094 ± .0074 |
| .383 | .8185 ± .0194 | .6897 ± .0163 | .8776 ± .0078 |
| .432 | .7978 ± .0144 | .6601 ± .0119 | .8631 ± .0060 |
| .482 | .7690 ± .0117 | .6181 ± .0094 | .8416 ± .0050 |
| .532 | .7321 ± .0103 | .5800 ± .0083 | .8203 ± .0047 |
| .582 | .7055 ± .0097 | .5468 ± .0077 | .8008 ± .0046 |
| .633 | .6826 ± .0097 | .5064 ± .0075 | .7765 ± .0048 |
| .682 | .6651 ± .0106 | .4827 ± .0081 | .7612 ± .0055 |
| .732 | .6776 ± .0141 | .4801 ± .0107 | .7619 ± .0072 |
| .781 | .6134 ± .0177 | .4415 ± .0139 | .7296 ± .0100 |
| .828 | .6844 ± .0318 | .4557 ± .0237 | .7501 ± .0166 |
| .873 | .5953 ± .0560 | .4369 ± .0435 | .7236 ± .0315 |
| .913 | .4742 ± .1128 | .3035 ± .0694 | .6019 ± .0706 |

Table 5.1: The ratios of the cross-sections per nucleon and $\alpha$ for $J/\psi$ production for the $x_F$ bins in each data set.

| SXF | | | |
|---|---|---|---|
| $\langle x_F \rangle$ | | $\sigma_W/\sigma_{Be}$ | $\alpha$ |
| -.068 | | .6837 ± .0491 | .8739 ± .0238 |
| -.020 | | .6709 ± .0272 | .8677 ± .0134 |
| .026 | | .7333 ± .0236 | .8972 ± .0106 |
| .075 | | .7532 ± .0253 | .9060 ± .0112 |
| .125 | | .7742 ± .0289 | .9151 ± .0124 |
| .174 | | .7502 ± .0422 | .9047 ± .0186 |
| .223 | | .7800 ± .0708 | .9176 ± .0301 |
| IXF | | | |
| $\langle x_F \rangle$ | $\sigma_{Fe}/\sigma_{Be}$ | $\sigma_W/\sigma_{Be}$ | $\alpha$ |
| .228 | .9465 ± .0887 | .7841 ± .0739 | .9236 ± .0311 |
| .277 | .9694 ± .0976 | .6937 ± .0772 | .8955 ± .0361 |
| .326 | .7620 ± .0982 | .8330 ± .1008 | .9331 ± .0399 |
| .377 | .9075 ± .1476 | .6412 ± .1165 | .8697 ± .0584 |
| .428 | 1.0773 ± .2085 | .7738 ± .1666 | .9317 ± .0704 |
| .480 | 1.2293 ± .3369 | .8310 ± .2536 | .9564 ± .1004 |
| LXF | | | |
| $\langle x_F \rangle$ | $\sigma_{Fe}/\sigma_{Be}$ | $\sigma_W/\sigma_{Be}$ | $\alpha$ |
| .332 | .8179 ± .0493 | .7086 ± .0435 | .8862 ± .0202 |
| .381 | .8100 ± .0394 | .6823 ± .0339 | .8745 ± .0163 |
| .431 | .8210 ± .0366 | .6761 ± .0309 | .8728 ± .0150 |
| .482 | .7964 ± .0364 | .6546 ± .0319 | .8619 ± .0158 |
| .532 | .7914 ± .0387 | .6806 ± .0343 | .8724 ± .0164 |
| .582 | .7782 ± .0458 | .5992 ± .0380 | .8358 ± .0204 |
| .632 | .6470 ± .0451 | .4498 ± .0363 | .7417 ± .0250 |
| .682 | .7235 ± .0706 | .4949 ± .0573 | .7810 ± .0360 |
| .732 | .5146 ± .0784 | .4390 ± .0679 | .7091 ± .0485 |
| .780 | .6218 ± .1177 | .4182 ± .0945 | .7189 ± .0688 |

Table 5.2: The ratios of the cross-sections per nucleon and $\alpha$ for $\psi'$ production for the $x_F$ bins in each data set.

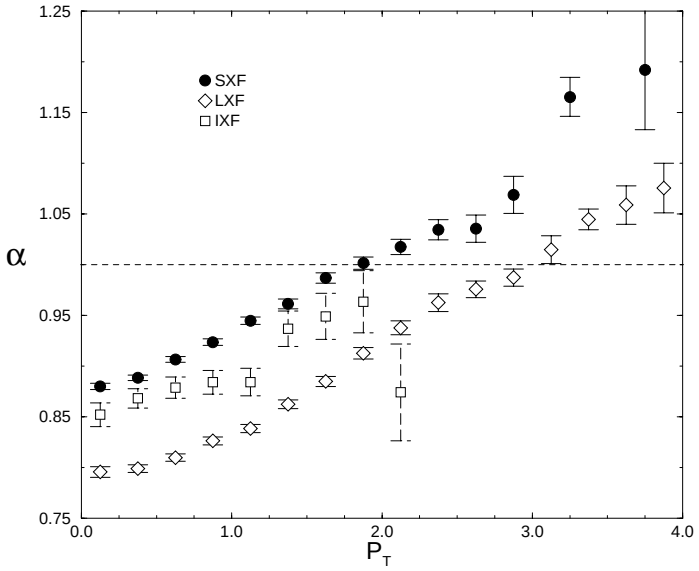


Figure 5.2: $\alpha$ versus $p_T$, in GeV/c, for $J/\psi$ production for the three data sets.

to $\alpha$ as demonstrated previously by other experiments and seen in Chapter 2. Since the $x_F$ dependence can easily be seen in the $p_T$ plot from observing the differences between the data sets, there may be a similar effect in the $x_F$ plot.

## 5.2 $P_T$ Correction

To determine if there is a bias caused by the $p_T$ acceptance in the $\alpha$ versus $x_F$ plot, the $p_T$ acceptance for each $x_F$ bin was studied. Some selected acceptances are shown in Figure 5.3. Not only are there differences in the $p_T$ acceptance between data sets, but there are also large acceptance differences between bins in the same data set. The largest effect is seen in the smallest $x_F$ bins.

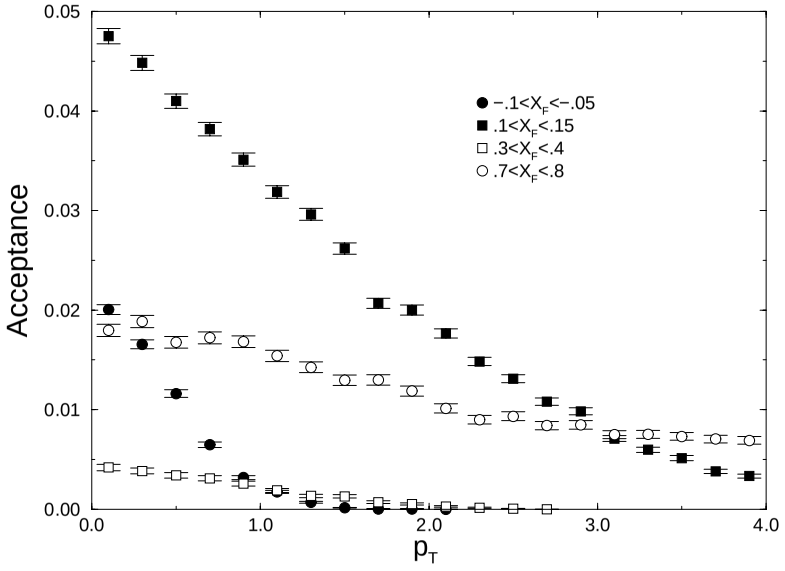


Figure 5.3: The acceptance versus $p_T$ for three different ranges of $x_F$. $p_T$ is given in GeV/c.

Since $\alpha$ has a strong dependence on $p_T$, different $p_T$ acceptances for the different $x_F$ bins will affect the value of $\alpha$ for that bin. If all of the $x_F$ bins had the same $p_T$ distributions, then the value of the ratios would be correct relative to each other. While for the majority of the E866 data the $p_T$ coverage is the same, at the smaller $x_F$ values and at the edges of the acceptance of each data set, the $p_T$ coverage becomes more limited. In order to remove this bias, a $p_T$ correction can be made. Since this is in effect an acceptance correction, it will be applied to the pseudo cross-sections, before the calculations of ratios or $\alpha$.

The first step in determining the $p_T$ correction is to calculate $\mathrm{d}\sigma/\mathrm{d}p_T^2$ for each target and data set for the $J/\psi$ and $\psi'$. Some examples of these curves can be seen

in Figure 5.4. These curves are then fit to the functional form,

$$d\sigma/dp_T^2 = A[1 + (p_T/p_0)^2]^{-6}. \quad (5.1)$$

Since the absolute normalization of these curves has not yet been performed, $A$ in the above equation is unimportant. In this correction, it is the shape of this function, determined from the value of $p_0$, which is important. The values of $p_0$ found in the fits for $J/\psi$ and $\psi'$ production for each target and data set can be found in Table 5.3. Due to the limited $p_T$ acceptance in the IXF data set, it was not possible to find $p_0$. For the IXF, the value for the LXF $J/\psi$ was used when calculating this correction. In addition to the functional form for the $p_T$ distributions, the functional form for $x_F$ is also needed which was found in E789 [48] as,

$$d\sigma/dx_F = A(1 - |x_F|)^B, \quad (5.2)$$

where $A$ was found to be 158 $\mu$b and $B$ was 5.09.

In order to study the acceptances of the E866 spectrometer, a large number of Monte Carlo events were generated for both the $J/\psi$ and $\psi'$, which can be used to determine the $p_T$ correction. These Monte Carlo events were generated with a flat $x_F$ and $p_T$ distribution, and then analyzed and placed into ntuples like the data. Since the Monte Carlo events were thrown flat in $x_F$ and $p_T$, they are reweighted

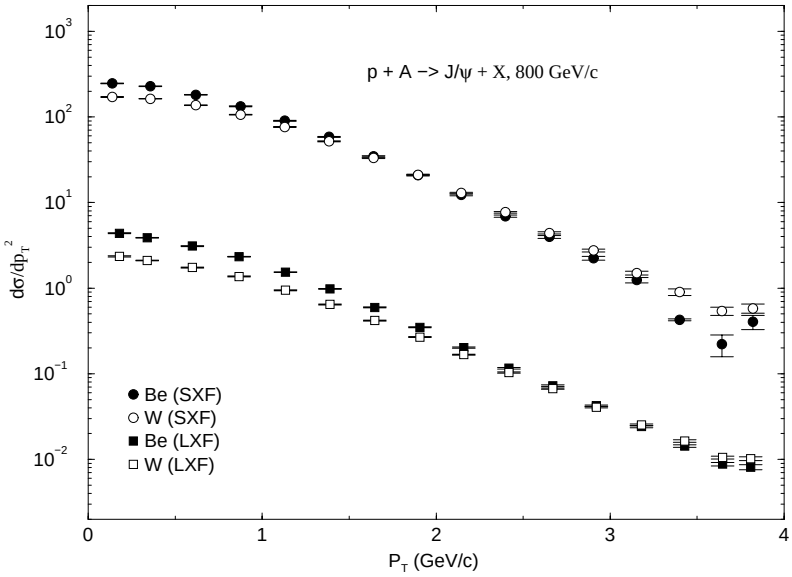


Figure 5.4: $d\sigma/dp_T^2$ versus $p_T$ for the beryllium and tungsten targets for the SXF and LXF data sets. $p_T$ is given in GeV/c and the units on the Y axis are arbitrary. The relative difference between the two data sets may also not be to scale.

| | | $J/\psi$ | $\psi'$ |
|---|---|---|---|
| Data Set | Target | $p_0$ | $p_0$ |
| SXF | Be | 2.542 | 2.821 |
| | W | 2.863 | 3.201 |
| LXF | Be | 2.632 | 2.733 |
| | Fe | 2.802 | 2.888 |
| | W | 2.921 | 3.036 |

Table 5.3: $p_0$ as determined from the fits to $\mathrm{d}\sigma/\mathrm{d}p_T^2$ as described in the text.

in $x_F$ and $p_T$ using the functional forms found above. The reweighting in $p_T$ used the $p_0$ value for the $J/\psi$ or $\psi'$ as appropriate, except as noted with the IXF. Then the Monte Carlo events were subjected to the same ntuple cuts as the data. The reweighted counts in each bin and target are then summed. A similar sum is then performed using a flat acceptance reweighted by $p_T$, which shows the ideal result for unity acceptance. The ratio of these two sums then provides the $p_T$ correction factor. This correction factor is calculated for both the $J/\psi$ and $\psi'$.

The pseudo cross-sections are modified by the $p_T$ correction factor and then can be used to calculate $\alpha$. The change in $\alpha$ from the $p_T$ correction is demonstrated in Figure 5.5. Here the three data sets have been combined for clarity. The largest correction can be seen in the smallest $x_F$ bins, as expected.

In order to test the corrections made, the cross-sections were again calculated, except this time an additional ntuple cut was used. All of the data was now restricted to $p_T < 1$, an area where there is good coverage in all $x_F$ bins. From this data $\alpha$ was calculated and can be seen in Figure 5.6[1] along with the $p_T$ corrected $\alpha$. Since the shapes of these two distributions are so similar, the $p_T$ correction appears appropriate.

It should be noted that while there is also a strong dependence in $x_F$, an $x_F$ correction to the $p_T$ plots does not need to be made. The SXF data set would appear to require a correction, since in this data set there is not the same $x_F$ acceptance in

[1]The values for $p_T < 1$ in this figure have a slightly different set of cuts in the LXF data set. The points are qualitatively correct.

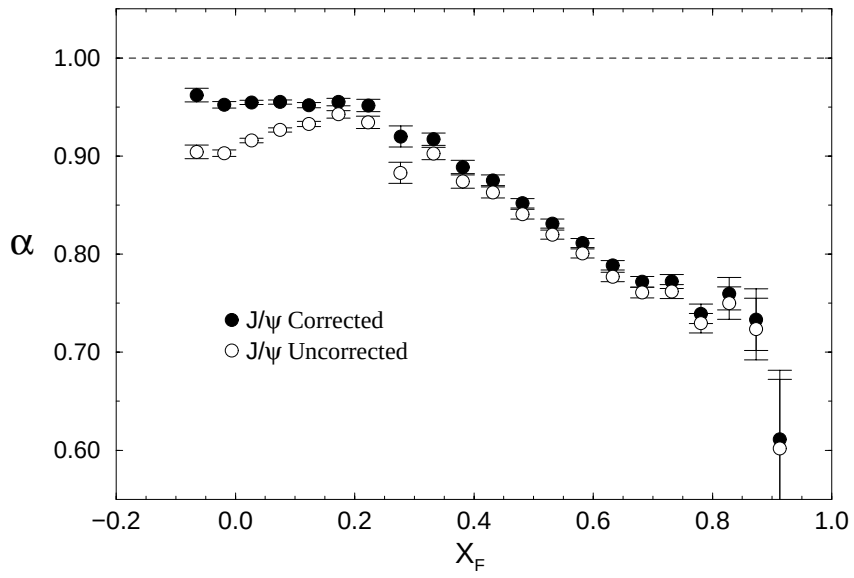


Figure 5.5: Nuclear dependence of $J/\psi$ production as corrected for the $p_T$ acceptance, closed circles, compared to the uncorrected, open circles.

each $p_T$ bin. However, $\alpha$ versus $x_F$ in this region, as seen in the corrected portion of Figure 5.6, is flat, so any correction would be negligible. In the IXF (for $p_T$ up to 2.0 GeV/c) and the LXF data sets, the $p_T$ bins have generally the same $x_F$ coverage, so any correction would just be an overall normalization and would not effect the shape of the curves.

## 5.3 Combining Data Sets

Now that the $p_T$ correction is made, the impact on the individual data sets can be observed. A plot of $\alpha$ versus $x_F$ corrected for $p_T$ acceptance is shown in Figure 5.7

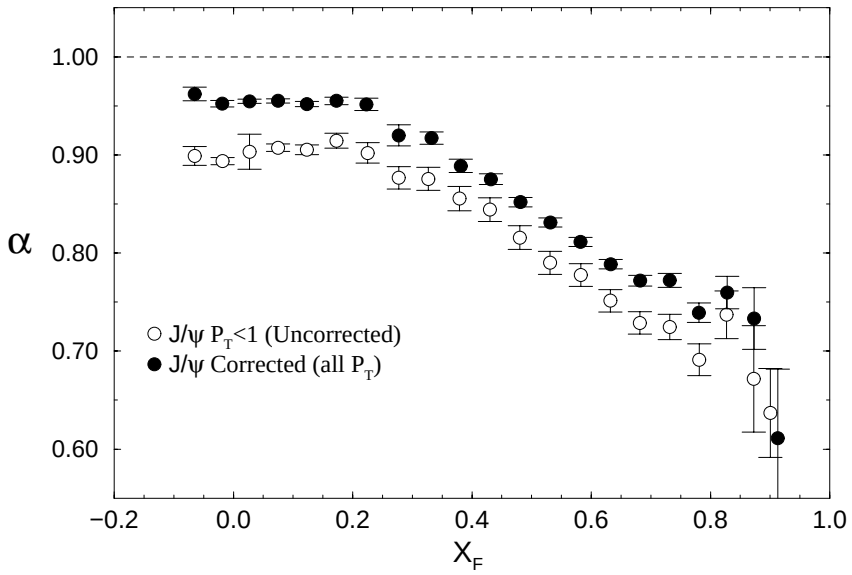


Figure 5.6: Nuclear dependence of $J/\psi$ production as corrected for the $p_T$ acceptance, closed circles, compared to the uncorrected which has been required to have a $p_T < 1$ GeV/c, open circles. The open circles have a slightly different set of cuts from the closed circles in the LXF data set, but are qualitatively correct.

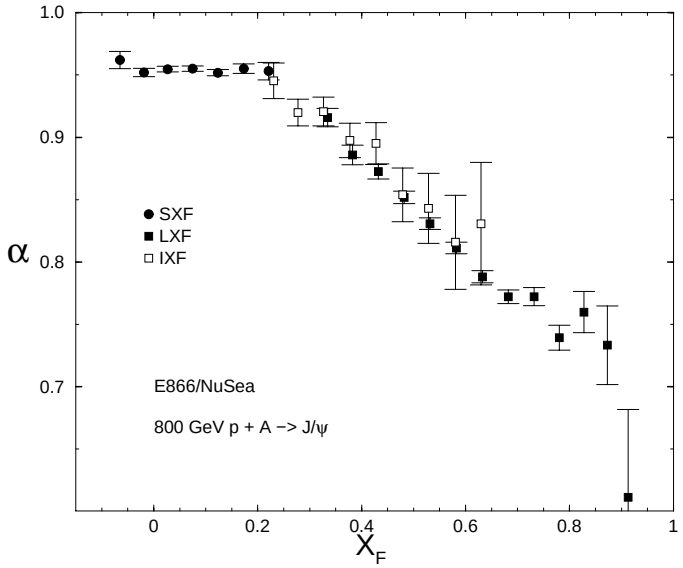


Figure 5.7: The nuclear dependence for the three different data sets corrected for $p_T$.

for the three data sets. The agreement between the SXF data set and the IXF data set is much improved. The values for $\alpha$ in Figure 5.7 and the corresponding target ratios for the $J/\psi$ and $\psi'$ are listed in Tables 5.4 and 5.5.

Since the three data sets are in agreement with each other, they are now combined. In the regions of $x_F$ where the points overlap, the data points are averaged, weighted by error.

| SXF $J/\psi$ | | |
|---|---|---|
| $\langle x_F \rangle$ | $\sigma_W/\sigma_{Be}$ | $\alpha$ |
| -.065 | .8921 ± .0186 | .9621 ± .0069 |
| -.019 | .8655 ± .0085 | .9521 ± .0033 |
| .027 | .8722 ± .0060 | .9547 ± .0023 |
| .075 | .8734 ± .0056 | .9551 ± .0022 |
| .124 | .8650 ± .0067 | .9519 ± .0026 |
| .173 | .8733 ± .0100 | .9551 ± .0038 |
| .221 | .8681 ± .0186 | .9531 ± .0071 |

| IXF $J/\psi$ | | | |
|---|---|---|---|
| $\langle x_F \rangle$ | $\sigma_{Fe}/\sigma_{Be}$ | $\sigma_W/\sigma_{Be}$ | $\alpha$ |
| .231 | .9041 ± .0398 | .8480 ± .0367 | .9454 ± .0143 |
| .277 | .8739 ± .0285 | .7835 ± .0256 | .9198 ± .0108 |
| .327 | .9088 ± .0316 | .7804 ± .0274 | .9207 ± .0115 |
| .377 | .8248 ± .0344 | .7346 ± .0309 | .8975 ± .0138 |
| .428 | .8397 ± .0424 | .7261 ± .0372 | .8950 ± .0168 |
| .479 | .8094 ± .0511 | .6349 ± .0418 | .8539 ± .0215 |
| .529 | .7893 ± .0647 | .6138 ± .0530 | .8430 ± .0280 |
| .581 | .7282 ± .0803 | .5702 ± .0668 | .8158 ± .0378 |
| .629 | .6085 ± .0908 | .6328 ± .0963 | .8307 ± .0492 |

| LXF $J/\psi$ | | | |
|---|---|---|---|
| $\langle x_F \rangle$ | $\sigma_{Fe}/\sigma_{Be}$ | $\sigma_W/\sigma_{Be}$ | $\alpha$ |
| .335 | .8608 ± .0221 | .7738 ± .0200 | .9158 ± .0074 |
| .383 | .8304 ± .0197 | .7072 ± .0168 | .8859 ± .0078 |
| .432 | .8112 ± .0146 | .6794 ± .0123 | .8726 ± .0060 |
| .482 | .7829 ± .0120 | .6374 ± .0097 | .8518 ± .0050 |
| .532 | .7457 ± .0185 | .5986 ± .0085 | .8307 ± .0047 |
| .582 | .7186 ± .0099 | .5642 ± .0079 | .8112 ± .0046 |
| .633 | .6968 ± .0099 | .5245 ± .0077 | .7881 ± .0048 |
| .682 | .6780 ± .0108 | .4988 ± .0084 | .7721 ± .0055 |
| .732 | .6901 ± .0144 | .4952 ± .0110 | .7721 ± .0072 |
| .781 | .6241 ± .0180 | .4546 ± .0144 | .7392 ± .0100 |
| .828 | .6963 ± .0323 | .4693 ± .0244 | .7598 ± .0166 |
| .873 | .6055 ± .0570 | .4497 ± .0448 | .7331 ± .0315 |
| .913 | .4821 ± .1146 | .3120 ± .0714 | .6111 ± .0706 |

Table 5.4: The ratios of the cross-sections per nucleon and $\alpha$ for $J/\psi$ production for the $x_F$ bins in each data set.

| SXF $\psi'$ | | | |
|---|---|---|---|
| $\langle x_F \rangle$ | | $\sigma_W/\sigma_{Be}$ | $\alpha$ |
| -.068 | | .8120 ± .0583 | .9309 ± .0238 |
| -.020 | | .7723 ± .0313 | .9143 ± .0134 |
| .026 | | .8149 ± .0262 | .9321 ± .0106 |
| .075 | | .8157 ± .0274 | .9324 ± .0112 |
| .125 | | .8171 ± .0306 | .9330 ± .0124 |
| .174 | | .7786 ± .0438 | .9170 ± .0186 |
| .223 | | .8028 ± .0729 | .9271 ± .0301 |
| IXF $\psi'$ | | | |
| $\langle x_F \rangle$ | $\sigma_{Fe}/\sigma_{Be}$ | $\sigma_W/\sigma_{Be}$ | $\alpha$ |
| .228 | .9937 ± .0931 | .8618 ± .0813 | .9545 ± .0311 |
| .277 | 1.0154 ± .1023 | .7589 ± .0845 | .9246 ± .0361 |
| .326 | .7993 ± .1030 | .9136 ± .1105 | .9635 ± .0399 |
| .377 | .9500 ± .1545 | .7006 ± .1272 | .8983 ± .0584 |
| .428 | 1.1257 ± .2179 | .8424 ± .1813 | .9593 ± .0704 |
| .480 | 1.2846 ± .3521 | .9048 ± .2761 | .9842 ± .1004 |
| LXF $\psi'$ | | | |
| $\langle x_F \rangle$ | $\sigma_{Fe}/\sigma_{Be}$ | $\sigma_W/\sigma_{Be}$ | $\alpha$ |
| .332 | .8293 ± .0500 | .7283 ± .0447 | .8952 ± .0202 |
| .381 | .8203 ± .0399 | .6995 ± .0348 | .8826 ± .0163 |
| .431 | .8314 ± .0371 | .6931 ± .0317 | .8808 ± .0150 |
| .482 | .8073 ± .0369 | .6724 ± .0327 | .8706 ± .0158 |
| .532 | .8026 ± .0393 | .6995 ± .0352 | .8813 ± .0164 |
| .582 | .7900 ± .0465 | .6171 ± .0391 | .8453 ± .0204 |
| .632 | .6563 ± .0457 | .4625 ± .0373 | .7506 ± .0250 |
| .682 | .7339 ± .0716 | .5088 ± .0589 | .7898 ± .0360 |
| .732 | .5219 ± .0795 | .4512 ± .0697 | .7179 ± .0485 |
| .780 | .6300 ± .1193 | .4291 ± .0969 | .7270 ± .0688 |

Table 5.5: The ratios of the cross-sections per nucleon and $\alpha$ for $\psi'$ production for the $x_F$ bins in each data set.

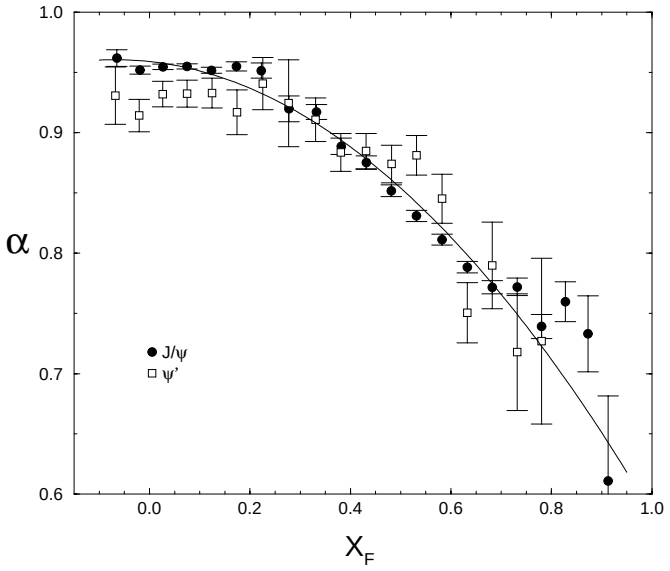


Figure 5.8: The $x_F$ nuclear dependence for $J/\psi$ and $\psi'$ production. The line represents a fit to the $J/\psi$ data as described in the text.

## 5.4 Final Results

The nuclear dependence for $J/\psi$ and the $\psi'$ production versus $x_F$ is shown in terms of $\alpha$ in Figure 5.8 and listed in Tables 5.6 and 5.7. The tables also list the mean $x_1$ and $x_2$ values for the given $x_F$ bins. The change in $\alpha$ due to the $p_T$ correction, $\Delta\alpha$, is also listed in the tables. For convenience, the $J/\psi$ data in Figure 5.8 have been fit with the simple parameterization:

$$\alpha(x_F) = 0.959(1 - 0.0467x_F - 0.345x_F^2). \tag{5.3}$$

While only second order, this parameterization provides a very good fit to the data.

| $J/\psi$ | | | | | |
|---|---|---|---|---|---|
| $\langle x_F \rangle$ | $\langle x_1 \rangle$ | $\langle x_2 \rangle$ | $\langle y_{CM} \rangle$ | $\alpha$ | $\Delta\alpha$ |
| -.0652 | .0534 | .1192 | -0.390 | .9621 ± .0069 | .0578 |
| -.0188 | .0706 | .0902 | -0.115 | .9521 ± .0033 | .0493 |
| .0269 | .0936 | .0679 | 0.1613 | .9547 ± .0023 | .0389 |
| .0747 | .1242 | .0511 | 0.4333 | .9551 ± .0022 | .0284 |
| .1235 | .1609 | .0395 | 0.6796 | .9519 ± .0026 | .0192 |
| .1729 | .2019 | .0316 | 0.8956 | .9551 ± .0038 | .0126 |
| .2228 | .2461 | .0262 | 1.0913 | .9516 ± .0064 | .0173 |
| .2772 | .2955 | .0213 | 1.2877 | .9198 ± .0108 | .0369 |
| .3324 | .3457 | .0182 | 1.4268 | .9173 ± .0062 | .0147 |
| .3812 | .3913 | .0160 | 1.5507 | .8888 ± .0068 | .0148 |
| .4316 | .4389 | .0142 | 1.6631 | .8753 ± .0056 | .0123 |
| .4815 | .4867 | .0128 | 1.7645 | .8519 ± .0049 | .0111 |
| .5314 | .5347 | .0117 | 1.8582 | .8310 ± .0046 | .0110 |
| .5823 | .5840 | .0107 | 1.9450 | .8112 ± .0046 | .0106 |
| .6325 | .6328 | .0098 | 2.0261 | .7885 ± .0048 | .0117 |
| .6821 | .6814 | .0092 | 2.0982 | .7718 ± .0054 | .0109 |
| .7316 | .7301 | .0086 | 2.1657 | .7721 ± .0072 | .0102 |
| .7806 | .7788 | .0080 | 2.2283 | .7392 ± .0100 | .0096 |
| .8278 | .8267 | .0076 | 2.2860 | .7598 ± .0166 | .0097 |
| .8731 | .8738 | .0072 | 2.3382 | .7331 ± .0315 | .0095 |
| .9128 | .9198 | .0070 | 2.3827 | .6111 ± .0706 | .0092 |

Table 5.6: The mean values of $x_1$, $x_2$, and $y_{CM}$ in $J/\psi$ production for each $x_F$ bin. $\alpha$ is also shown along with $\Delta\alpha$, where $\Delta\alpha$ is the difference between the corrected $\alpha$ and the uncorrected $\alpha$.

| | | | $\psi'$ | | |
|---|---|---|---|---|---|
| $\langle x_F \rangle$ | $\langle x_1 \rangle$ | $\langle x_2 \rangle$ | $\langle y_{CM} \rangle$ | $\alpha$ | $\Delta\alpha$ |
| -.0679 | .0665 | .1346 | -0.344 | .9309 ± .0238 | .0570 |
| -.0203 | .0848 | .1056 | -0.104 | .9143 ± .0134 | .0466 |
| .0261 | .1079 | .0828 | 0.132 | .9321 ± .0106 | .0349 |
| .0749 | .1378 | .0645 | 0.369 | .9324 ± .0112 | .0264 |
| .1243 | .1734 | .0513 | 0.588 | .9330 ± .0124 | .0179 |
| .1739 | .2130 | .0418 | 0.785 | .9170 ± .0186 | .0123 |
| .2252 | .2573 | .0347 | 0.974 | .9408 ± .0216 | .0203 |
| .2766 | .3031 | .0293 | 1.144 | .9246 ± .0361 | .0291 |
| .3305 | .3511 | .0253 | 1.281 | .9109 ± .0181 | .0143 |
| .3806 | .3971 | .0223 | 1.401 | .8838 ± .0157 | .0097 |
| .4310 | .4441 | .0199 | 1.512 | .8848 ± .0146 | .0091 |
| .4817 | .4919 | .0179 | 1.614 | .8741 ± .0156 | .0094 |
| .5315 | .5394 | .0163 | 1.705 | .8813 ± .0164 | .0089 |
| .5820 | .5879 | .0150 | 1.791 | .8453 ± .0204 | .0095 |
| .6323 | .6364 | .0138 | 1.869 | .7506 ± .0250 | .0089 |
| .6823 | .6852 | .0129 | 1.942 | .7898 ± .0360 | .0088 |
| .7317 | .7336 | .0120 | 2.009 | .7179 ± .0485 | .0088 |
| .7803 | .7818 | .0113 | 2.071 | .7270 ± .0688 | .0081 |

Table 5.7: The mean values of $x_1$, $x_2$, and $y_{CM}$ in $\psi'$ production for each $x_F$ bin. $\alpha$ is also shown along with $\Delta\alpha$, where $\Delta\alpha$ is the difference between the corrected $\alpha$ and the uncorrected $\alpha$.

The nuclear dependence versus $p_T$ for $J/\psi$ and $\psi'$ production is shown in terms of $\alpha$ in Figure 5.9. The values for $\alpha$ can also be found in Tables 5.8 and 5.9, while the corresponding ratios are found in Tables 5.8 and 5.10.

Figure 5.9 shows the nuclear dependence for each of the three data sets, as well as the results versus $p_T$ for NA3 [25]. In all four of these plots essentially the same increase for both the $J/\psi$ and $\psi'$ is seen. A second order parameterization was used to fit the curves of each data set, with only the overall normalization allowed to change between data sets. This parameterization was found to be:

$$\alpha(p_T) = A_i(1 + 0.0599p_T + 0.0108p_T^2). \tag{5.4}$$

where $A_i = 0.870, 0.840.$ and $0.783$ for the SXF, IXF, and LXF data sets, respectively. These fits are shown as the solid lines on Figure 5.9. The NA3 data can also be well fit using the above parameterization. The results are also shown in the figure with $A_i = 0.881$.

## 5.5 Systematic Uncertainties

The advantage of taking a ratio is that many of the uncertainties cancel, which greatly reduces the systematic error. Alternating the targets in the wheel also removes problems that occur over a long time scale. Here the main contributions for systematic

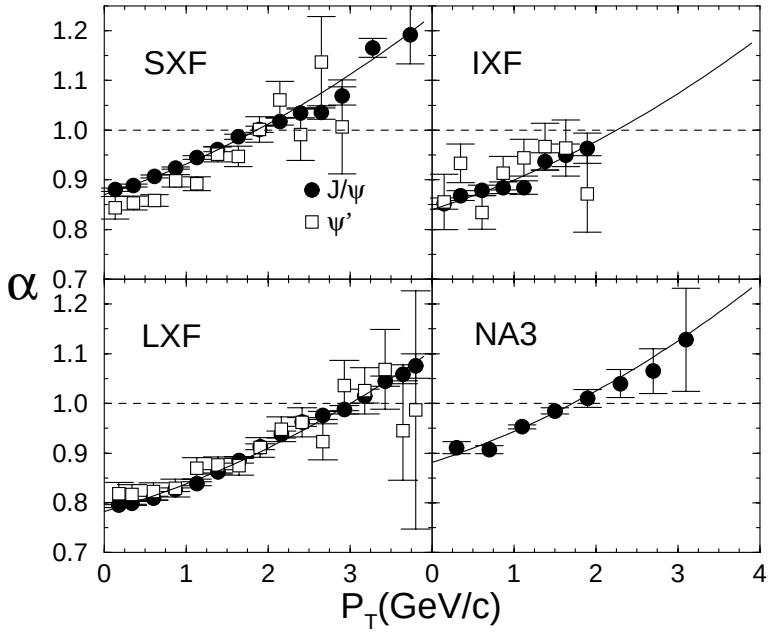


Figure 5.9: The $p_T$ nuclear dependence for $J/\psi$ and $\psi'$ production. The data sets are labeled as shown. The lower right plot is the NA3 [25] 200 GeV proton induced data converted to $\alpha$. The lines represents a fit to the $J/\psi$ data as described in the text.

| SXF | | | | |
|---|---|---|---|---|
| | $J/\psi$ | | $\psi'$ | |
| $\langle p_T \rangle$ | $\sigma_W/\sigma_{Be}$ | $\alpha$ | $\sigma_W/\sigma_{Be}$ | $\alpha$ |
| .137 | .6965 ± .0065 | .8800 ± .0031 | .6239 ± .0431 | .8436 ± .0229 |
| .357 | .7143 ± .0056 | .8884 ± .0026 | .6419 ± .0269 | .8530 ± .0139 |
| .617 | .7542 ± .0064 | .9065 ± .0028 | .6525 ± .0236 | .8584 ± .0120 |
| .875 | .7946 ± .0077 | .9237 ± .0024 | .7348 ± .0274 | .8978 ± .0118 |
| 1.130 | .8464 ± .0094 | .9447 ± .0037 | .7227 ± .0302 | .8923 ± .0139 |
| 1.384 | .8896 ± .0129 | .9612 ± .0048 | .8634 ± .0404 | .9513 ± .0155 |
| 1.640 | .9612 ± .0147 | .9869 ± .0051 | .8522 ± .0519 | .9470 ± .0202 |
| 1.894 | 1.0044 ± .0185 | 1.0015 ± .0061 | 1.0032 ± .0776 | 1.0011 ± .0256 |
| 2.145 | 1.0543 ± .0243 | 1.0175 ± .0076 | 1.2015 ± .1343 | 1.0609 ± .0371 |
| 2.399 | 1.1092 ± .0331 | 1.0344 ± .0099 | .9725 ± .1510 | .9907 ± .0523 |
| 2.649 | 1.1130 ± .0448 | 1.0355 ± .0134 | 1.5097 ± .4185 | 1.1366 ± .0919 |
| 2.903 | 1.2305 ± .0677 | 1.0688 ± .0182 | 1.0194 ± .2898 | 1.0064 ± .0943 |
| 3.276 | 1.6378 ± .0939 | 1.1654 ± .0192 | | |
| 3.734 | 1.7780 ± .3130 | 1.1919 ± .0588 | | |

Table 5.8: The ratios of the cross-sections per nucleon and $\alpha$'s for $J/\psi$ and $\psi'$ production for the $p_T$ bins in the SXF data set.

| IXF | | |
|---|---|---|
| | $J/\psi$ | $\psi'$ |
| $\langle p_T \rangle$ | $\alpha$ | $\alpha$ |
| .151 | .8521 ± .0117 | .8554 ± .0555 |
| .350 | .8682 ± .0096 | .9330 ± .0386 |
| .610 | .8788 ± .0105 | .8342 ± .0337 |
| .869 | .8840 ± .0118 | .9132 ± .0335 |
| 1.122 | .8842 ± .0135 | .9444 ± .0368 |
| 1.380 | .9368 ± .0174 | .9668 ± .0468 |
| 1.632 | .9490 ± .0227 | .9638 ± .0562 |
| 1.895 | .9635 ± .0307 | .8718 ± .0769 |
| 2.141 | .8741 ± .0478 | 1.1494 ± .1388 |
| LXF | | |
| | $J/\psi$ | $\psi'$ |
| $\langle p_T \rangle$ | $\alpha$ | $\alpha$ |
| .178 | .7956 ± .0053 | .8185 ± .0222 |
| .339 | .7990 ± .0038 | .8169 ± .0197 |
| .600 | .8097 ± .0036 | .8227 ± .0175 |
| .869 | .8262 ± .0038 | .8295 ± .0181 |
| 1.130 | .8385 ± .0040 | .8695 ± .0216 |
| 1.387 | .8623 ± .0043 | .8761 ± .0162 |
| 1.645 | .8848 ± .0049 | .8744 ± .0185 |
| 1.903 | .9127 ± .0057 | .9114 ± .0199 |
| 2.160 | .9377 ± .0069 | .9480 ± .0247 |
| 2.414 | .9625 ± .0088 | .9620 ± .0292 |
| 2.670 | .9758 ± .0082 | .9230 ± .0363 |
| 2.930 | .9873 ± .0084 | 1.0359 ± .0508 |
| 3.182 | 1.0148 ± .0137 | 1.0256 ± .0466 |
| 3.427 | 1.0447 ± .0102 | 1.0685 ± .0803 |
| 3.647 | 1.0588 ± .0190 | .9453 ± .1001 |
| 3.801 | 1.0755 ± .0245 | .9868 ± .2398 |

Table 5.9: $\alpha$ for $J/\psi$ and $\psi'$ production for the $p_T$ bins in the IXF and LXF data sets.

| IXF | | | | |
|---|---|---|---|---|
| | $J/\psi$ | | $\psi'$ | |
| $\langle p_T \rangle$ | $\sigma_{Fe}/\sigma_{Be}$ | $\sigma_W/\sigma_{Be}$ | $\sigma_{Fe}/\sigma_{Be}$ | $\sigma_W/\sigma_{Be}$ |
| .151 | .7943 ± .0279 | .6346 ± .0227 | .6660 ± .1204 | .6654 ± .1133 |
| .350 | .8187 ± .0239 | .6673 ± .0195 | .9990 ± .1123 | .7972 ± .0939 |
| .610 | .8083 ± .0258 | .6926 ± .0220 | .8230 ± .0778 | .5825 ± .0613 |
| .869 | .8489 ± .0303 | .6994 ± .0250 | .9433 ± .1033 | .7571 ± .0773 |
| 1.122 | .8205 ± .0241 | .6998 ± .0292 | .9250 ± .0951 | .8416 ± .0941 |
| 1.380 | .9083 ± .0481 | .8239 ± .0436 | 1.1312 ± .1534 | .8796 ± .1250 |
| 1.632 | .9346 ± .0649 | .8544 ± .0588 | .9054 ± .1584 | .8998 ± .1531 |
| 1.895 | .9373 ± .0653 | .8949 ± .0834 | .8023 ± .1300 | .6704 ± .1636 |
| 2.141 | .7149 ± .1031 | .6967 ± .1013 | .4069 ± .3035 | 1.5025 ± .6300 |

| LXF | | | | |
|---|---|---|---|---|
| | $J/\psi$ | | $\psi'$ | |
| $\langle p_T \rangle$ | $\sigma_{Fe}/\sigma_{Be}$ | $\sigma_W/\sigma_{Be}$ | $\sigma_{Fe}/\sigma_{Be}$ | $\sigma_W/\sigma_{Be}$ |
| .178 | .6983 ± .0104 | .5380 ± .0082 | .7008 ± .0475 | .5828 ± .0417 |
| .339 | .7084 ± .0078 | .5427 ± .0061 | .7932 ± .0331 | .5566 ± .0259 |
| .600 | .7187 ± .0079 | .5615 ± .0062 | .7388 ± .0286 | .5820 ± .0238 |
| .869 | .7419 ± .0084 | .5902 ± .0067 | .7526 ± .0298 | .5931 ± .0249 |
| 1.130 | .7648 ± .0091 | .6117 ± .0074 | .7918 ± .0339 | .6736 ± .0296 |
| 1.387 | .8049 ± .0104 | .6569 ± .0085 | .8038 ± .0396 | .6867 ± .0348 |
| 1.645 | .8291 ± .0117 | .7042 ± .0100 | .7744 ± .0426 | .6890 ± .0389 |
| 1.903 | .8678 ± .0137 | .7667 ± .0121 | .8876 ± .0592 | .7584 ± .0522 |
| 2.160 | .9077 ± .0166 | .8270 ± .0151 | .8822 ± .0720 | .8577 ± .0691 |
| 2.414 | .9659 ± .0206 | .8894 ± .0192 | .9563 ± .0884 | .8865 ± .0828 |
| 2.670 | .9896 ± .0249 | .9274 ± .0234 | .9381 ± .1048 | .7782 ± .0920 |
| 2.930 | .9815 ± .0290 | .9619 ± .0282 | 1.1466 ± .1834 | 1.1024 ± .1787 |
| 3.182 | 1.0636 ± .0394 | 1.0435 ± .0385 | 1.0673 ± .1792 | 1.0696 ± .1801 |
| 3.427 | 1.0882 ± .0516 | 1.1445 ± .0530 | 1.3875 ± .3176 | 1.2295 ± .2880 |
| 3.647 | 1.1910 ± .0728 | 1.1930 ± .0725 | .8812 ± .2433 | .8249 ± .2386 |
| 3.801 | 1.2380 ± .0996 | 1.2561 ± .1000 | .6910 ± .3150 | .8684 ± .3929 |

Table 5.10: The ratios of the cross-sections per nucleon for $J/\psi$ and $\psi'$ production for the $p_T$ bins in the IXF and LXF data sets.

| Source | Data Set | | |
|---|---|---|---|
| | SXF | IXF | LXF |
| target thickness | 0.5 | 0.3 | 0.3 |
| rate dependence | 0.5 | 0.5 | 0.5 |
| target Z acceptance | 0.1 | 0.1 | 0.1 |
| beam attenuation | 0.3 | 0.3 | 0.3 |
| overall uncorrected | 0.77 | 0.66 | 0.66 |

Table 5.11: Contributions to the systematic uncertainty for the uncorrected ratio for $J/\psi$ production by data set measured in percent. The overall values give the total systematic uncertainty except for the uncertainty in the $p_T$ correction which is discussed in the text.

error occur due to differences in the targets.

Even in a ratio, there are still sources of systematic uncertainty which can not be ignored. In this experiment they are target thickness, rate dependence, target Z acceptance, beam attenuation, and the $p_T$ acceptance correction. The contribution from each of these sources except $p_T$ acceptance is shown in Table 5.11, and its variance with data set.

The target thickness uncertainty is mainly due to the Be target which had a larger uncertainty than the other targets. Since the Be target is covered in Kapton tape, the thickness of the tape makes the measurement uncertain by 0.01 inch. The Fe and W targets do not have this problem. The rate dependence uncertainty comes from acceptance differences due to beam intensity. A nice discussion of rate dependence can be found in [8]. Since the Be target is much thicker than the others, its mounting

method placed the Z position of its center farther downstream than the other targets. This caused a small target Z acceptance uncertainty, which was estimated from a Monte Carlo study using different target positions.

The overall systematic uncertainty is determined by adding the individual contributions in quadrature. For ratios which have not been corrected for $p_T$ acceptance and for ratios versus $p_T$ the systematic uncertainty is only on the order of 0.8%. In general, the uncertainty for $\alpha$ is the uncertainty for the ratio reduced by a factor of three. So, the systematic uncertainty for uncorrected values of $\alpha$ is only around 0.3%.

When looking at the $p_T$ corrected ratios, the systematic uncertainty for the $p_T$ correction which is $x_F$ and particle dependent, has to be taken into account. For the SXF data set this uncertainty is 2.4% in the lowest $x_F$ bin and falls to 0.2% in the highest for $J/\psi$ production, while for the $\psi'$, the uncertainty has a maximum of 3.9% and a minimum of 0.8%. For the IXF data set, the uncertainty for the $J/\psi$ is 2.6% falling to 1.8%. The uncertainty for the $\psi'$ in the IXF is essentially flat at 1.8%. The uncertainty in the LXF data set is approximately flat over all $x_F$ for both particles at about 0.3% for the $J/\psi$ and the $\psi'$. The systematic uncertainty for the $p_T$ correction is then added in quadrature to the rest of the uncertainty to get the overall systematic uncertainty shown in Table 5.12.

| Charmonia | Ratio | $\alpha$ |
|---|---|---|
| $J/\psi$ | 2.5 | 0.84 |
| $\psi'$ | 4.0 | 1.3 |

Table 5.12: The overall systematic uncertainty for the corrected ratios and $\alpha$'s for $J/\psi$ and $\psi'$ production measured in percent.

## 5.6 Observations

### 5.6.1 $J/\psi$ and $\psi'$

As seen in Figure 5.8, for $x_F$ less than 0.25, $\alpha$ for the $J/\psi$ is at its largest value and relatively flat. As $x_F$ increases above 0.25, $\alpha$ decreases sharply. The $\psi'$ is also at its maximum and flat in alpha at low $x_F$, but this appears to extend out to near $x_F$ of 0.5 before $\alpha$ begins to decrease to that of the $J/\psi$. Most significant is that $\alpha$ for the $\psi'$ for $x_F$ less than 0.25 is less than $\alpha$ for the $J/\psi$. However since $\alpha$ for the $J/\psi$ begins to decrease at $x_F = 0.25$, the $\psi'$ appears to become less suppressed than the $J/\psi$ for the region $0.4 < x_F < 0.5$.

This region of $0.4 < x_F < 0.5$ may not be as big an effect as it appears in Figure 5.8. In calculating $x_F$ for the $J/\psi$, the physical mass of the $J/\psi$ is used, likewise for the $\psi'$. Since the $c\bar{c}$ pair should be unaware of the particle to which it will hadronize, it is the $c\bar{c}$ pair and its mass that is relevant to the nuclear interaction. The mass difference between the two particles can be removed by looking at the nuclear

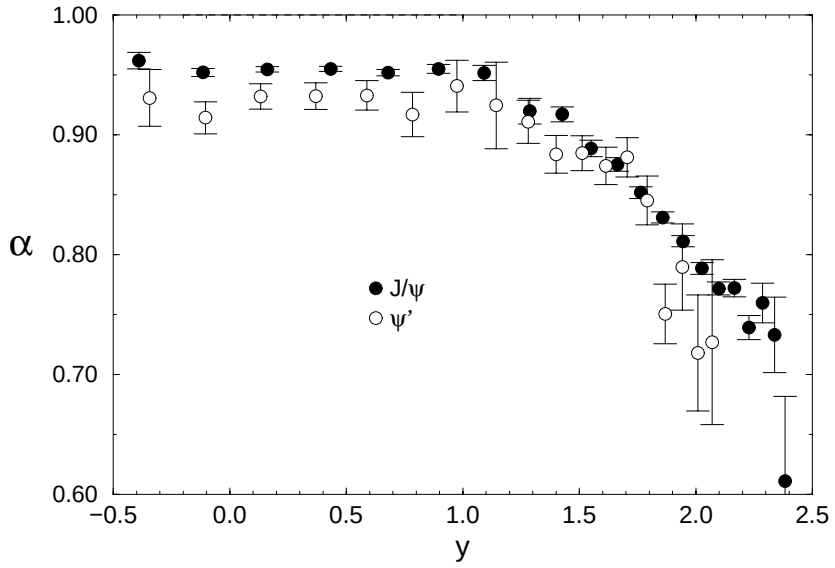


Figure 5.10: The center-of-mass rapidity nuclear dependence for $J/\psi$ and $\psi'$ production.

dependence versus the center-of-mass rapidity, $y$, instead of $x_F$. This is shown in Figure 5.10, and here the region where the $J/\psi$ becomes more suppressed than the $\psi'$ disappears.

The shapes of the curves for the nuclear dependence versus $p_T$ are in general similar for the $J/\psi$ and $\psi'$ in the various data sets, as shown in Figure 5.9. There are still slight differences. The $\psi'$ is slightly more suppressed than the $J/\psi$ in the SXF data set, which is sensible since the $\psi'$ is more suppressed in the $x_F$ plot as well. The IXF data set exhibits a slightly less suppressed $\psi'$ than $J/\psi$. This is also seen in $\alpha$ versus $x_F$. Still the $\psi'$ shapes are similar. The $p_T$ shape for the $J/\psi$ is similar across the data sets, which can be seen by the fits in the figure. The NA3 data also show

the same shape, even though it was produced at 200 GeV.

### 5.6.2 Other Experiments

A comparison of E866 to some of the experiments listed in Chapter 2 is shown in Figure 5.11. The data from the 200 GeV NA3 experiment match the 800 GeV E866 data well. This would imply that charmonia suppression scales with $x_F$. The data from the 800 GeV E772 [20] and E789 [26] experiments do not match up with the E866 data mainly in the regions of $x_F < 0.3$. As seen in Figure 2.5, both E772 and E789 had a severe restriction of their $p_T$ acceptance. It is expected that if the E772 and E789 data were corrected for their $p_T$ acceptance, they would agree with the E866 data. On the other hand, the large $x_F$ results from E789[27] (shown in Figure 2.4) appear to be high by more than their systematic uncertainty of 2.5%, possibly due to errors in the relative normalization between the E789 Be and Cu targets.

## 5.7 Nuclear Effects Revisited

The E866 experiment was performed in order to provide additional data in hopes of better understanding the nuclear effects that produce the observed nuclear suppression. The higher statistics and wider kinematic coverage was expected to put some limits on the many nuclear effects. Now that the data have been presented, the nuclear effects from Chapter 2 will now be revisited to see what can be learned.

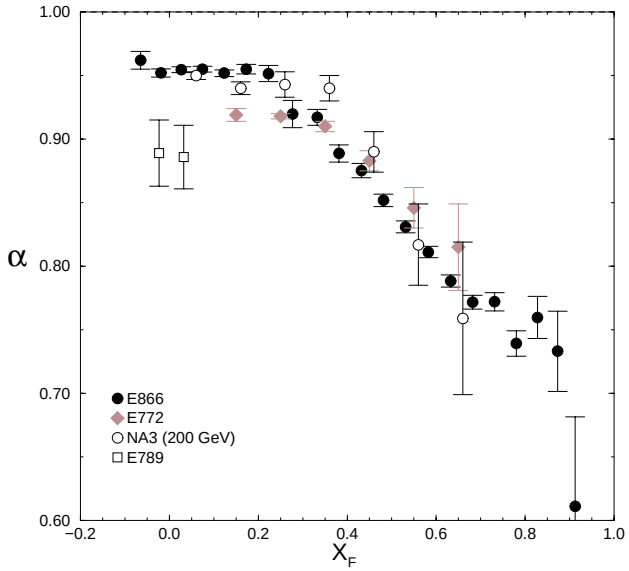


Figure 5.11: $\alpha$ versus $x_F$ for E866 compared to Experiments NA3 [25], E772 [20], and E789 [26].

### 5.7.1 Absorption

Absorption is any mechanism which will reduce the charmonia cross-section in a heavier nucleus. The main component of absorption is the disassociation of the $c\bar{c}$ pair due to interactions with the nuclear medium which would likely cause the individual $c$ and $\bar{c}$ to hadronize into $D$ mesons. Since we see in Figure 5.8 that the maximum $\alpha$ is around 0.95, all of the $x_F$ bins demonstrate some suppression. Therefore some absorption must occur.

The increased suppression of the $\psi'$ over the $J/\psi$ at small $x_F$ would also imply some final state absorption. If the $c\bar{c}$ were to hadronize while still in the nuclear medium, then the physical size of the two states would cause their absorption to differ. The larger $\psi'$ should have a greater cross-section for absorption, and should be more greatly suppressed, which is what is seen. However, even for an atom as large as tungsten, it is only the negative $x_F$ regions and those close to $x_F = 0$ where the $c\bar{c}$ should hadronize in the nucleus. The addition of comovers will move this region farther into the positive, but it is thought to be unlikely that comovers in $pA$ collisions could extend this effect out to $x_F = 0.3$ where the increased suppression is still seen.

In general it is not thought that the large suppression at high $x_F$ can be explained by absorption. However the SUBATECH group [49] have suggested that if the color octet lifetime is short, there may be this kind of strong absorption. Since the lifetime

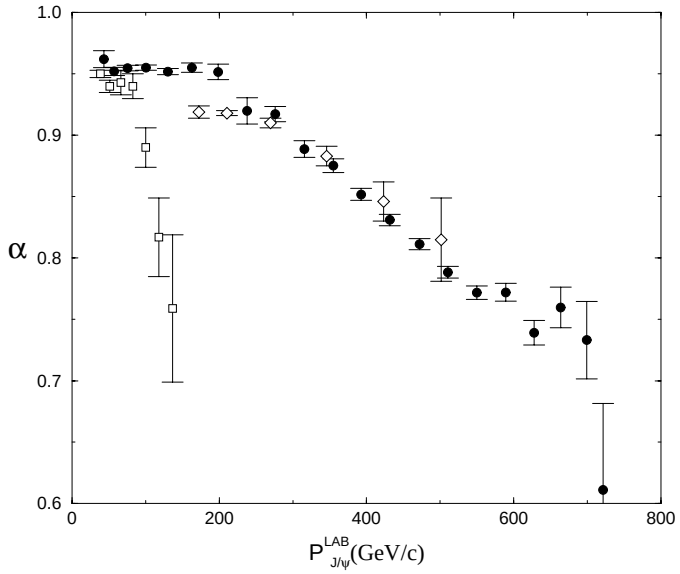


Figure 5.12: $\alpha$ versus $p_{J/\psi}^{LAB}$ for E866 compared to Experiments NA3 [25] and E772 [20].

in the laboratory frame would increase due to Lorenz dilation at larger $x_F$ values, the lifetime of the octet state and thus the amount of absorption would also increase with $x_F$. However, such an explanation is inconsistent with the lack of scaling with $p_{J/\psi}^{LAB}$. As seen in Figure 5.12, this scaling already breaks down for $p_{J/\psi}^{LAB} > 90$ GeV/c, which corresponds to $x_F > 0.05$.

### 5.7.2 Shadowing

As mentioned before, the reduction of the nuclear structure function at low $x_2$ due to shadowing could cause a suppression of charmonia at large $x_F$. Current estimates [33,

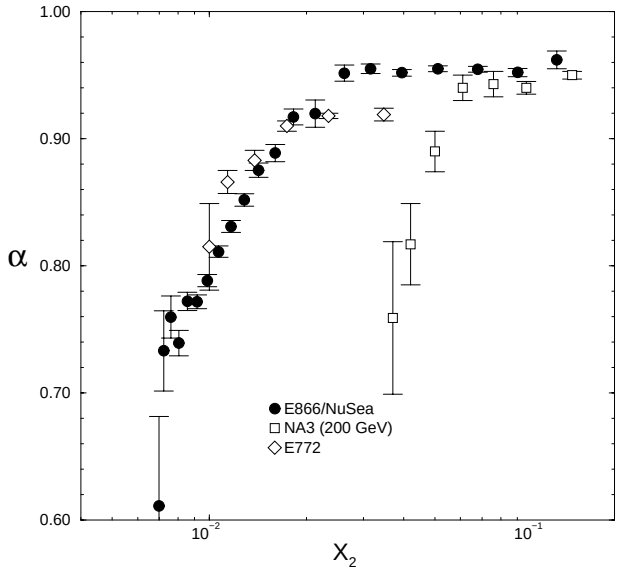


Figure 5.13: $\alpha$ versus $x_2$ for E866 compared to Experiments NA3 [25] and E772 [20].

17] based on phenomenological fits to a broad range of data including deep inelastic scattering experiments, only predict a few percent suppression. While small, this will still contribute to the E866 data, but the suppression seen versus $x_F$ is much larger than a few percent. The lack of scaling in $x_2$, Figure 5.13, will also prevent shadowing from explaining the majority of the suppression in $x_F$.

### 5.7.3 Energy Loss

Energy loss is an effect that could be used to explain the increased suppression at large $x_F$. Since energy loss would decrease the forward momentum of the particle, the events in the higher $x_F$ bins would be shifted to lower bins, and would show up

as a suppression. This can occur in all phases of charmonia production, from initial to final state.

In initial state energy loss the incoming parton can interact with nuclear matter and lose energy. This should affect both the $J/\psi$ and the $\psi'$ equally, so it will be unable to explain the small $x_F$ increased suppression, but the more important effect for initial state energy loss should be at larger $x_F$ where there is increased suppression and the $J/\psi$ and $\psi'$ are more equally suppressed. As mentioned before Drell-Yan would be a good measure of initial state energy loss, since the final state in Drell-Yan does not interact strongly in the nuclear medium. While the charmonia may experience energy loss from an initial state gluon instead of a quark, Gavin and Milana [12] predict that the gluon's energy loss would only be greater than that of a quark by a color factor of 9/4.

Since the LXF data set also contained a large number of Drell-Yan dimuons, this data set was used to study [10] initial state energy loss. A portion of the result is shown in Figure 5.14. This figure breaks up the data by $x_2$ into a shadowing region ($x_2 < 0.036$) and a non-shadowing region. By looking at this and the difference between the prediction curves and the points, it is obvious that shadowing leaves little room for suppression due to energy loss.

Final state energy loss, i.e. energy loss due to the formed $J/\psi$ or $\psi'$, may also explain the suppression at large $x_F$. The problem here is that by the time the

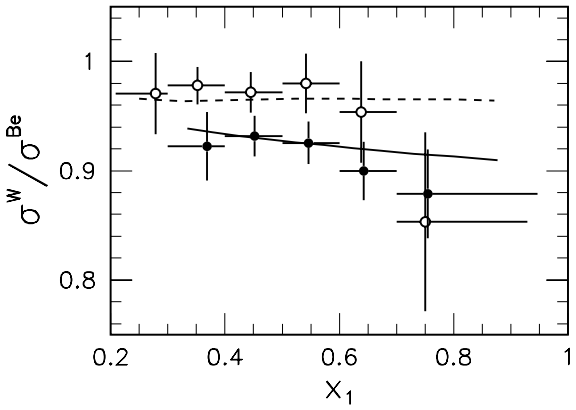


Figure 5.14: Ratios of the measured Drell-Yan cross-section per nucleon for W/Be versus $x_1$. The solid (open) circles are those events with $x_2$ less than (greater than) 0.036, and the solid (dashed) curve is the corresponding shadowing prediction. [10]

charmonia is formed at large $x_F$ it has already left the nucleus. Also if final state energy loss was the cause of the suppression, the nuclear dependence at large $x_F$ should be independent of the beam particle. Figure 2.1 showed that this is not the case.

Finally there could be energy loss due to the intermediate $c\bar{c}$ pair. Gavin and Milana [12] treat the color octet $c\bar{c}$ pair similarly to a gluon, so then the initial state arguments above apply. If the $c\bar{c}$ pair is in a color singlet state, then it is thought to interact minimally, so energy loss should not have a large effect. In order for this intermediate state energy loss to have the large effect shown at large $x_F$, the interaction cross-section for the $c\bar{c}$ state would have to be much larger than presently thought.

## 5.8 Conclusion

A measurement of the nuclear dependence for $J/\psi$ and $\psi'$ production has been achieved over a greater kinematic range and accuracy than any other experiment. A difference in $J/\psi$ and $\psi'$ production was seen for the first time in $pA$ collisions at negative $x_F$. At this time, the suppression versus $x_F$ seen by E866 can not be explained by any single nuclear effect or combination of nuclear effects. So while this data may rule out some nuclear effects, it is clear that present models will need to be modified or new models will need to be created to explain the data. E866 was a success.

# Bibliography


[1] J.A. Crittenden *et al.*, [E605 Collaboration], Phys. Rev. **D34**, 2584 (1986).

[2] G. Moreno *et al.*, [E605 Collaboration], Phys. Rev. **D43**, 2815 (1991).

[3] D.M. Alde *et al.*, [E772 Collaboration], Phys. Rev. Lett. **64**, 2479 (1990).

[4] D.M. Jansen *et al.*, [E789 Collaboration], Phys. Rev. Lett. **74**, 3118 (1995)

[5] E.A. Hawker *et al.* [FNAL E866/NuSea Collaboration], Phys. Rev. Lett. **80**, 3715 (1998).

[6] J.C. Peng *et al.* [FNAL E866/NuSea Collaboration], Phys. Rev. **D58**, 092004 (1998)

[7] E. A. Hawker, Ph.D. Thesis, Texas A&M University, (1998).

[8] R. S. Towell, Ph.D. Thesis, University of Texas, (1999).

[9] T. H. Chang, Ph.D. Thesis, New Mexico State University, (1999).

[10] M. A. Vasiliev *et al*, [FNAL E866/NuSea Collaboration], Phys. Rev. Lett. **83**, 2304 (1999).

[11] T. Matsui and H. Satz, Phys. Lett. **B178**, 416 (1986).

[12] S. Gavin and J. Milana, Phys. Rev. Lett. **68**, 1834 (1992).

[13] S.J. Brodsky and P. Hoyer, Phys. Lett. **B298**, 165 (1993).

[14] R. Baier, Y.L. Dokshitzer, A.H. Mueller, S. Peigne and D. Schiff, Nucl. Phys. **B484**, 265 (1997).

[15] R. Baier, Y.L. Dokshitzer, A.H. Mueller and D. Schiff, Nucl. Phys. **B531**, 403 (1998).

[16] S.J. Brodsky, P. Hoyer, C. Peterson and N. Sakai, Phys. Lett. **B93**, 451 (1980).

[17] K.J. Eskola, V.J. Kolhinen and C.A. Salgado, Eur. Phys. J. **C9**, 61 (1999).

[18] S. Gavin and R. Vogt, Nucl. Phys. **B345**, 104 (1990).

[19] M. Beneke and I.Z. Rothstein, Phys. Rev. **D54**, 2005 (1996).

[20] D.M. Alde *et al.*, [E772 Collaboration], Phys. Rev. Lett. **66**, 133 (1991).

[21] M.C. Abreu *et al.* [NA50 Collaboration], CERN-EP-99-013, Accepted by Phys. Lett. B).

[22] J.E. Augustin *et al.*, Phys. Rev. Lett. **33**, 1406 (1974).

[23] J.J. Aubert *et al.*, Phys. Rev. Lett. **33**, 1404 (1974).

[24] G.S. Abrams *et al.*, Phys. Rev. Lett. **33**, 1453 (1974).

[25] J. Badier *et al.* [NA3 Collaboration], Z. Phys. **C20**, 101 (1983).

[26] M.J. Leitch *et al.*, [E789 Collaboration], Phys. Rev. **D52**, 4251 (1995).

[27] M.S. Kowitt *et al.*, [E789 Collaboration], Phys. Rev. Lett. **72**, 1318 (1994).

[28] M.J. Leitch *et al.* [E789 Collaboration], Phys. Rev. Lett. **72**, 2542 (1994).

[29] G.A. Alves *et al.* [Fermilab E769 Collaboration], Phys. Rev. Lett. **70**, 722 (1993).

[30] M. Adamovich *et al.* [BEATRICE Collaboration], Nucl. Phys. **B495**, 3 (1997).

[31] M.C. Abreu *et al.* [NA38 Collaboration], Phys. Lett. **B444**, 516 (1998).

[32] M.C. Abreu *et al.* [NA51 Collaboration], Phys. Lett. **B438**, 35 (1998).

[33] R. Vogt, hep-ph/9907317.

[34] G.A. Schuler and R. Vogt, Phys. Lett. **B387**, 181 (1996).

[35] G.A. Schuler, hep-ph/9403387.

[36] A. Sansoni [CDF Collaboration], Nuovo Cim. **109A**, 827 (1996).

[37] R. Gavai, D. Kharzeev, H. Satz, G.A. Schuler, K. Sridhar and R. Vogt, Int. J. Mod. Phys. **A10**, 3043 (1995).

[38] L. Antoniazzi *et al.* [E705 Collaboration], Phys. Rev. Lett. **70**, 383 (1993).

[39] J.J. Aubert *et al.* [European Muon Collaboration], Phys. Lett. **123B**, 275 (1983).

[40] A. Bodek *et al.*, Phys. Rev. Lett. **50**, 1431 (1983).

[41] P. Amaudruz *et al.* [New Muon Collaboration], Nucl. Phys. **B441**, 3 (1995).

[42] M.R. Adams *et al.* [E665 Collaboration], Phys. Rev. Lett. **68**, 3266 (1992).

[43] S.J. Brodsky and P. Hoyer, Phys. Rev. Lett. **63**, 1566 (1989).

[44] C. Caso *et al.*, Eur. Phys. J. **C3**, 1 (1998).

[45] C. A. Gagliardi, E. A. Hawker, R. E. Tribble, D. D. Koetke, P. M. Nord, P. L. McGaughey, and C. N. Brown, Nucl. Instrum. Methods, A **418** 322 (1998).

[46] CN/ASD Group. *PAW users guide, CERN Program Library Q121.* CERN, 1995.

[47] CN/ASD Group. *HBOOK Reference Manual, CERN Program Library Y250.* CERN, 1998.

[48] M.H. Schub *et al.* [E789 Collaboration], Phys. Rev. **D52**, 1307 (1995).

[49] F. Arleo, P.B. Gossiaux, T. Gousset and J. Aichelin, hep-ph/9907286.